

Spectroscopic characterization of the $a^3\Pi$ state of aluminum monofluoride

Cite as: J. Chem. Phys. **156**, 124306 (2022); <https://doi.org/10.1063/5.0082601>

Submitted: 16 December 2021 • Accepted: 21 February 2022 • Accepted Manuscript Online: 22 February 2022 • Published Online: 24 March 2022

 N. Walter,  M. Doppelbauer,  S. Marx, et al.



View Online



Export Citation



CrossMark

ARTICLES YOU MAY BE INTERESTED IN

[Photodissociation dynamics of \$N_3^+\$](#)

The Journal of Chemical Physics **156**, 124307 (2022); <https://doi.org/10.1063/5.0085081>

[Chlorine dioxide: An exception that proves the rules of localized chemical bonding](#)

The Journal of Chemical Physics **156**, 124303 (2022); <https://doi.org/10.1063/5.0084739>

[A deep potential model with long-range electrostatic interactions](#)

The Journal of Chemical Physics **156**, 124107 (2022); <https://doi.org/10.1063/5.0083669>

Lock-in Amplifiers
up to 600 MHz



Zurich
Instruments



Spectroscopic characterization of the $a^3\Pi$ state of aluminum monofluoride

Cite as: J. Chem. Phys. 156, 124306 (2022); doi: 10.1063/5.0082601

Submitted: 16 December 2021 • Accepted: 21 February 2022 •

Published Online: 24 March 2022



View Online



Export Citation



CrossMark

N. Walter,^{1,a)} M. Doppelbauer,¹ S. Marx,¹ J. Seifert,¹ X. Liu,¹ J. Pérez-Ríos,¹ B. C. Sartakov,² S. Truppe,¹ and G. Meijer^{1,b)}

AFFILIATIONS

¹Fritz-Haber-Institut der Max-Planck-Gesellschaft, Faradayweg 4-6, 14195 Berlin, Germany

²Prokhorov General Physics Institute, Russian Academy of Sciences, Vavilovstreet 38, 119991 Moscow, Russia

^{a)}Author to whom correspondence should be addressed: walter@fhi-berlin.mpg.de

^{b)}Electronic mail: meijer@fhi-berlin.mpg.de

ABSTRACT

Spectroscopic studies of aluminum monofluoride (AlF) have revealed its highly favorable properties for direct laser cooling. All Q lines of the strong $A^1\Pi \leftarrow X^1\Sigma^+$ transition around 227 nm are rotationally closed and thereby suitable for the main cooling cycle. The same holds for the narrow, spin-forbidden $a^3\Pi \leftarrow X^1\Sigma^+$ transition around 367 nm, which has a recoil limit in the μK range. We here report on the spectroscopic characterization of the lowest rotational levels in the $a^3\Pi$ state of AlF for $v = 0-8$ using a jet-cooled, pulsed molecular beam. An accidental AC Stark shift is observed on the $a^3\Pi_0, v = 4 \leftarrow X^1\Sigma^+, v = 4$ band. By using time-delayed ionization for state-selective detection of the molecules in the metastable $a^3\Pi$ state at different points along the molecular beam, the radiative lifetime of the $a^3\Pi_1, v = 0, J = 1$ level is experimentally determined as $\tau = 1.89 \pm 0.15$ ms. A laser/radio frequency multiple resonance ionization scheme is employed to determine the hyperfine splittings in the $a^3\Pi_1, v = 5$ level. The experimentally derived hyperfine parameters are compared to the outcome of quantum chemistry calculations. A spectral line with a width of 1.27 kHz is recorded between hyperfine levels in the $a^3\Pi, v = 0$ state. These measurements benchmark the electronic potential of the $a^3\Pi$ state and yield accurate values for the photon scattering rate and for the elements of the Franck-Condon matrix of the $a^3\Pi-X^1\Sigma^+$ system.

© 2022 Author(s). All article content, except where otherwise noted, is licensed under a Creative Commons Attribution (CC BY) license (<http://creativecommons.org/licenses/by/4.0/>). <https://doi.org/10.1063/5.0082601>

I. INTRODUCTION

Ultracold atomic physics created new opportunities in precision metrology, quantum science, and fundamental physics.¹ The application of cooling techniques to molecules—although more challenging to implement due to the more complex energy level structure of molecules—allows for full control over their motions and interactions and to study chemistry in a new regime.^{2,3} Ongoing applications include high resolution spectroscopy to determine the possible variation of fundamental constants⁴ and the electric dipole moment of elementary particles.⁵⁻⁸ Future applications in the quantum simulation of mathematically inaccessible many body systems and quantum computing are anticipated.⁹⁻¹¹

Among the various diatomic molecules that are being used in laser cooling experiments, aluminum monofluoride (AlF) has particularly favorable properties. It is strongly bound and can be

efficiently produced. The photon scattering rate on the $A^1\Pi \leftarrow X^1\Sigma^+$ electronic transition is exceptionally large, and the vibrationally off-diagonal Einstein A coefficients are orders of magnitude smaller than the diagonal ones. Moreover, all Q lines of a $^1\Pi \leftarrow ^1\Sigma^+$ transition are rotationally closed. These favorable properties were already noted when a list of diatomic molecules was compiled for this purpose in 2004, but then, it was remarked that AlF is only the most promising molecule when leaving “experimental convenience aside.”¹² What makes laser cooling of AlF experimentally inconvenient is that the strong $A^1\Pi \leftarrow X^1\Sigma^+$ cooling transition is in the deep UV at around 227 nm. Moreover, both nuclei have nuclear spin, with a value of 5/2 for ²⁷Al and 1/2 for ¹⁹F, yielding a complicated hyperfine structure.

Recently, narrowband cw laser systems in the deep UV with a power of several 100 mW have become commercially available. The hyperfine structure in the lowest rotational levels of the $X^1\Sigma^+$,

$A^1\Pi$, and $a^3\Pi$ states of AlF has been experimentally determined in the required detail.¹³ Efficient optical cycling has been demonstrated on various Q lines of the $A^1\Pi \leftarrow X^1\Sigma^+$ transition.¹⁴ The main vibrationally off-diagonal Einstein A coefficient is experimentally found to be about 300 times smaller than the diagonal one, making laser cooling with a single repump laser feasible. While the $A^1\Pi \leftarrow X^1\Sigma^+$ transition allows large optical scattering forces to be generated, it has a comparatively high Doppler cooling limit of several mK. The $a^3\Pi \leftarrow X^1\Sigma^+$ transition around 367 nm is also vibrationally highly

diagonal, but its laser cooling limit is the recoil limit, which lies in the μK range.¹⁵ Laser cooling can be achieved by cycling on any of the Q_2 lines and on the (considerably weaker) $P_1(1)$ line.

To be able to accurately determine the Franck–Condon factors for the $a^3\Pi \leftarrow X^1\Sigma^+$ transition, both potential energy curves, as extracted from experimental data, need to be accurately known. For the $X^1\Sigma^+$ electronic ground state, an accurate potential has been reported.¹⁶ By contrast, the available rotationally resolved spectroscopic data on the $a^3\Pi$ state are insufficient and limited to the lowest two vibrational states.^{17–19} This makes the $a^3\Pi$ state the least well characterized one of the low-lying electronically excited states of AlF until now. The lifetimes of the rotational levels in the $a^3\Pi$ state are strongly Ω -, J -, and parity-dependent.²⁰ To determine the photon scattering rate, the radiative lifetimes of the rotational levels in the $a^3\Pi$ state need to be measured.

In this paper, we present a spectroscopic investigation of AlF in a supersonically cooled, pulsed molecular beam. Different excitation and detection schemes are applied, as indicated in Fig. 1. One-color (1 + 2) REMPI detection via the $b^3\Sigma^+$, $v = 0 \leftarrow a^3\Pi$, $v = 0$ band is used to determine the lifetimes of the rotational levels in the $a^3\Pi$, $v = 0$ state. Laser induced phosphorescence detection and two-color (1 + 1') REMPI is applied to determine the energies of the lowest rotational levels up to $v = 7$. The vibrational, rotational, and spin–orbit coupling parameters of the $a^3\Pi$ state are extracted. All Λ -doublet transitions within the $a^3\Pi_1$, $v = 5$, $J = 1$ level are recorded, and the hyperfine parameters are derived. Their values are compared to the outcome of *ab initio* calculations. The precise knowledge of the hyperfine structure of the $a^3\Pi_1$, $v = 5$, $J = 1$ level is crucial for the study of the singlet–triplet doorway levels that arise from the interaction of the $A^1\Pi$, $v = 6$ and the $b^3\Sigma^+$, $v = 5$ states. A detailed, hyperfine resolved study of these doorway levels will be separately reported upon.²¹

II. EXPERIMENTAL SETUP

The experimental setup is shown schematically in Fig. 2. A pulsed solenoid valve (General Valve, Series 9) releases short gas pulses (duration about 50 μs , 10 Hz repetition rate) through a circular orifice into a narrow channel with a conical nozzle. The gas is composed of 2% SF_6 seeded in a noble gas with a backing pressure of 3 bar. In the channel, the injected gas pulse passes over a rotating aluminum rod that is irradiated by a Q-switched Nd:YAG laser (1064 nm, 16 mJ pulse energy). Ablated aluminum atoms react with SF_6 to form AlF, and these molecules, mixed in the carrier gas, then expand from the nozzle (defined as $z = z_0 = 0$) into the source chamber.

In the supersonic expansion, AlF is translationally and internally cooled through collisions with the carrier gas. Typical translational and rotational temperatures are $T_{\text{transl}} \approx 3$ K and $T_{\text{rot}} \approx 5$ K. Due to the conditions during the production process and the relatively inefficient cooling of vibrations, the molecules are distributed over several vibrational levels of the $X^1\Sigma^+$ electronic ground state.¹⁹ This is important for our study of higher vibrational levels of the metastable $a^3\Pi$ state since only transitions of the $a^3\Pi \leftarrow X^1\Sigma^+$ band with $\Delta v = 0$ are sufficiently strong. The population of the lowest three vibrational levels can be characterized by a vibrational temperature $T_{\text{vib}} \approx 700$ K, but the higher vibrational levels up to $v = 7$ remain populated by $\sim 1\%$. AlF is almost exclusively present

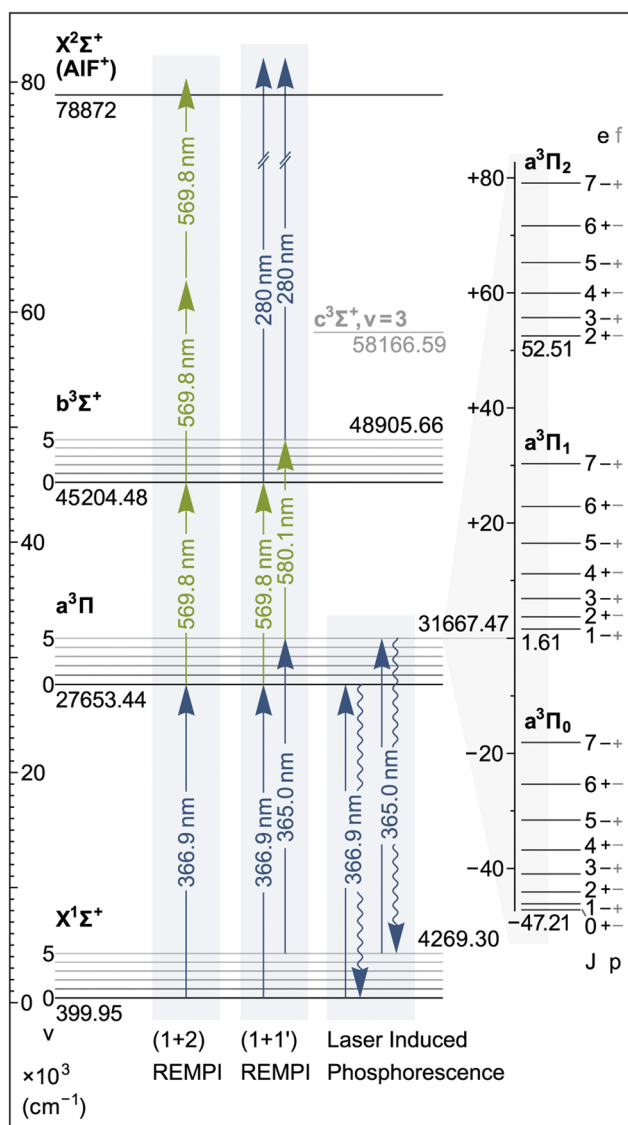


FIG. 1. Scheme of the electronic, vibrational, and rotational levels of AlF that are relevant in this study. The rotational structure of the three Ω manifolds of the $a^3\Pi$ state is shown on an expanded scale. For $\Omega = 0$, the e and f levels are split by about 10 GHz; only the e levels have been probed. The excitation and detection schemes that are applied are indicated. In all experiments, AlF is excited on the $\Delta v = 0$ bands of the $a^3\Pi \leftarrow X^1\Sigma^+$ transition and thus prepared in selected vibrational and rotational levels of the metastable $a^3\Pi$ state.

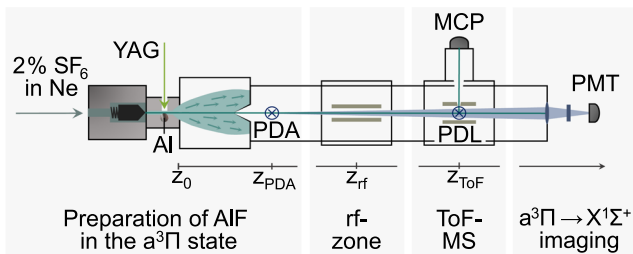


FIG. 2. Schematic view of the modular supersonic molecular beam setup. AIF is produced in a chemical reaction of laser-ablated aluminum atoms and SF₆ and is excited further downstream to the metastable a³Π state. Subsequent excitation by laser or radio frequency radiation and detection takes place in spatially separated regions.

in the electronic ground state with a very small fraction in the first electronically excited, metastable triplet state.

The supersonic expansion results in the formation of an AIF-seeded molecular beam, whose forward velocity is primarily determined by that of the carrier gas. For the lifetime measurements (see Sec. VI), different noble gases are used as carrier gas in order to manipulate the beam velocity. Unless stated otherwise, all other experiments are carried out using neon, yielding a beam velocity of roughly 750 m/s. The molecular beam is collimated through a conically shaped skimmer with a 4 mm diameter opening. The coordinate z (see Fig. 2) is defined along the axis of the molecular beam through the array of several differentially pumped vacuum chambers ($\sim 10^{-6}$ mbar). At various positions z further downstream, the AIF molecules interact with laser and/or radio frequency (rf) radiation that crosses the molecular beam perpendicularly.

At $z = z_{\text{PDA}} = 25$ cm, AIF is resonantly excited from the X¹Σ⁺ electronic ground state to selected rovibrational levels of the a³Π state. For this, a frequency-doubled pulsed dye amplifier (PDA), operated with pyridine 2 dye, is used. The PDA is pumped by a frequency-doubled Nd:YAG laser and injection seeded with a tunable, narrowband, and cw TiSa laser. The absolute frequency of the TiSa seed-laser is measured with a wavemeter (HighFinesse WS8, 10 MHz accuracy). The PDA contains a phase-conjugate mirror based on stimulated Brillouin scattering (SBS), and the frequency shift imposed by the SBS cell to the pulsed radiation (at the fundamental frequency) is experimentally determined to be $-1.98(5)$ GHz. The frequency-doubled laser pulses in the 365–367 nm range have about 10 mJ energy. The spectral profile of this laser system is inferred by recording the a³Π₀, $J = 0 \leftarrow X^1\Sigma^+$, $J = 1$ transition of AIF. The hyperfine splitting of both the ground and excited levels of this transition (12 and 3 MHz, respectively) is negligible compared to the laser linewidth. The measured spectral line shape of this P₁(1) line shows a near-Gaussian main peak with a full width at half maximum (FWHM) of 220 MHz, reflecting the intrinsic bandwidth of the laser system. In addition, a minor side peak with the same width, centered about 350 MHz higher in frequency, is observed. This side peak results from an adjacent longitudinal mode of the TiSa seed-laser and is taken into account in the data analysis.

The AIF molecules in the a³Π state can be directly detected by monitoring the a³Π → X¹Σ⁺ phosphorescence that occurs along the

molecular beam for $z \geq z_{\text{PDA}}$. For this, an on-axis light collection system is installed at the end of the molecular beam machine and the phosphorescence is imaged on a photomultiplier tube (PMT). As the solid angle for light collection is larger when the molecules are closer to the on-axis detector, the phosphorescence signal is peaked several hundred μs after laser excitation. A bandpass filter centered around 367 nm in front of the PMT suppresses scattered light from the laser ablation source and ambient light.

Since all rotational levels in the a³Π state have a radiative lifetime of more than a millisecond, subsequent excitation and detection can take place in spatially separated regions, further downstream. Their arrangement is modular and adapted to the requirements of the individual experiments. In the rf interaction zone, transitions between opposite parity Λ-doublet components within a certain J level in the a³Π state are driven by exposing the molecules to rf radiation in the 1–500 MHz range.

Parity-selective detection of the molecules in the a³Π state is implemented by using resonant ionization via rotational levels of the b³Σ⁺ state. The AIF⁺ cations are mass-selectively detected using a linear Wiley–McLaren time-of-flight mass spectrometer (ToF-MS). Two counter-propagating, collimated beams (a few mm diameter) of two pulsed dye lasers (PDLs) intersect the molecular beam between the extraction electrodes of the ToF-MS.

As seen in Fig. 1, two different ionization schemes are applied. The first one is two-color resonance enhanced multiphoton ionization [(1 + 1') REMPI]. The radiation of the first PDL (sub-mJ pulse energy, 5 ns pulse duration, 570–580 nm) resonantly excites the molecules from the a³Π state to a particular rovibrational level in the b³Σ⁺ state. The radiative lifetime of these levels is about 190 ns.²² Within tens of ns, the molecules are ionized by a single photon of a second PDL (5 mJ pulse energy, 5 ns pulse duration, 280 nm). In the second scheme, AIF molecules in the a³Π state are detected via single-color (1 + 2) REMPI via the b³Σ⁺ state. For this, only the PDL in the visible, i.e., for the b³Σ⁺ ← a³Π transition, is used but operated at higher pulse energies (5–10 mJ).

The (1 + 1') REMPI scheme is used to record spectra with high resolution since the pulse energy of the resonant excitation laser can be kept low and power broadening is suppressed. The main advantage of using the (1 + 2) REMPI scheme is that with only the unfocused, visible laser present, the AIF⁺ cation is the only ion produced, enabling highly sensitive detection. We observe that (1 + 2) REMPI only works for the b³Σ⁺, $\nu = 0 \leftarrow a^3\Pi$, $\nu = 0$ band. We assume that in that case, the required intermediate level for the near-resonant two-photon ionization step (around 62 755.5 cm⁻¹ above the minimum of the X¹Σ⁺ state potential) is a highly excited vibrational level of the c³Σ⁺ state. The (1 + 2) REMPI scheme is exclusively used for the lifetime measurement of the a³Π, $\nu = 0$ state, as a high spectral resolution is not needed for this.

In order to ensure field-free excitation and ionization, the voltages on the extraction electrodes are switched on a few hundred ns after the ionization process is completed. The positively charged parent ions are then accelerated perpendicular to the plane spanned by the molecular beam and laser beams, i.e., vertically, toward two chevron mounted microchannel plates (dual MCP detector). The voltages are switched off directly after the AIF⁺ ions have left the acceleration region, thereby spreading out higher mass ions over a wide range of arrival times. Deflection electrodes are mounted in the field-free flight path of the ToF setup, and their voltage is switched

to deflect all ions that are lighter than AlF^+ . The output of the MCP is amplified and read into a computer using a high-speed digitizer card (NI PXIe-5160, maximum sample rate 2.5 GS/s).

III. MOLECULAR HAMILTONIAN

The Hamiltonian used to describe the energy level structure of AlF can be written in a general form as

$$H = H_{\text{ev}} + H_{\text{rot}} + H_{\text{fs}} + H_{\text{hfs}} \quad (1)$$

and is presented and discussed in detail elsewhere.^{13,22} In those earlier studies, the last two terms of Eq. (1) are used to determine the fine structure and hyperfine structure parameters for the $a^3\Pi$, $A^1\Pi$, and $b^3\Sigma^+$ states. Here, we focus on the first two terms of Eq. (1), the electronic and vibrational part of the Hamiltonian H_{ev} and the rotational part H_{rot} . Generally, the energies of the vibrational levels for a given electronic state are expressed as²³

$$E_{\text{vib}}(\nu) = T_e + \omega_e \left(\nu + \frac{1}{2} \right) - \omega_e x_e \left(\nu + \frac{1}{2} \right)^2 + \omega_e y_e \left(\nu + \frac{1}{2} \right)^3 + \omega_e z_e \left(\nu + \frac{1}{2} \right)^4, \quad (2)$$

where T_e is the minimum of the electronic potential and ω_e is the fundamental vibrational energy with the subsequent higher order correction terms $\omega_e x_e$, $\omega_e y_e$, and $\omega_e z_e$, all given in wavenumbers. A comprehensive compilation of values for these parameters for the known electronic states of AlF is given elsewhere.^{17,24}

The rotational part of the Hamiltonian for the levels in the $a^3\Pi$ state is approximated by

$$H_{\text{rot}} = \tilde{A}_\nu (\mathbf{L} \cdot \mathbf{S}) + B_\nu (\mathbf{J} - \mathbf{L} - \mathbf{S})^2, \quad (3)$$

where \tilde{A}_ν is an effective electron spin-orbit coupling constant and B_ν is the rotational constant for level ν , \mathbf{J} is the angular momentum of the molecule, \mathbf{L} is the total orbital angular momentum of electron motion, and \mathbf{S} is the total spin of the electrons. We use an effective electron spin-orbit constant \tilde{A}_ν , as only e levels can be measured in the $a^3\Pi_0$ manifold; there is insufficient information on the terms in the fine structure part of the Hamiltonian that contribute to the splitting between these e levels and the levels in the $a^3\Pi_1$ manifold. In a good approximation, the relation between the actual spin-orbit coupling constant A_ν and the effective constant \tilde{A}_ν used here is given by

$$A_\nu \approx \tilde{A}_\nu + 2\lambda_\nu - (o_\nu + p_\nu + q_\nu). \quad (4)$$

The fine structure parameters λ_ν for the spin-spin interaction and o_ν , p_ν , and q_ν for the Λ -doubling are only known for the $\nu = 0$ level of the $a^3\Pi$ state,^{13,22} where the relation $A_0 \approx \tilde{A}_0 + 590$ MHz holds. In this approximation, minor effects due to the spin-rotation interaction parameter γ_ν are neglected.¹³ For the vibrational dependence of \tilde{A}_ν and B_ν , we use the following expressions:

$$\tilde{A}_\nu = \tilde{A}_e - \tilde{\zeta}_e \left(\nu + \frac{1}{2} \right) + \tilde{\eta}_e \left(\nu + \frac{1}{2} \right)^2, \quad (5)$$

$$B_\nu = B_e - \alpha_e \left(\nu + \frac{1}{2} \right) + \beta_e \left(\nu + \frac{1}{2} \right)^2. \quad (6)$$

With $A_0/B_0 \approx 85$, the $a^3\Pi$ state is close to Hund's case (a). Both Λ and Σ , the projections of \mathbf{L} and \mathbf{S} on the internuclear axis, are well defined, as is their sum $\Omega = \Lambda + \Sigma$. The spin-orbit interaction splits the $a^3\Pi$ state into three Ω manifolds, and the energies of the low- J rotational levels are given by the eigenvalues of the rotational Hamiltonian matrix

$$\begin{pmatrix} -\tilde{A}_\nu + B_\nu(x+1) & -B_\nu\sqrt{2x} & 0 \\ -B_\nu\sqrt{2x} & B_\nu(x+1) & -B_\nu\sqrt{2(x-2)} \\ 0 & -B_\nu\sqrt{2(x-2)} & \tilde{A}_\nu + B_\nu(x-3) + c_\nu \end{pmatrix} \quad (7)$$

with $x = J(J+1)$. The correction term $c_\nu = 4\lambda_\nu - (o_\nu + p_\nu + q_\nu)$ is needed because of the use of \tilde{A}_ν instead of A_ν and is kept fixed at $c_\nu = c_0 = 2\lambda_0 + 590$ MHz. The first, second, and third row and column have the wavefunctions for $\Omega = 0, 1, \text{ and } 2$ as basis. Λ -doubling in the $\Omega = 1$ and 2 manifolds is neglected. Commonly, an additional offset term B_ν is added to the diagonal elements of the matrix,^{25,26} but here, we follow the convention used in earlier studies on AlF by Brown *et al.*¹⁸ Note that in this case also the term $-4/3\lambda_\nu$ is absorbed in the value of T_e .

The $X^1\Sigma^+$ and the $b^3\Sigma^+$ states are best described by Hund's case (b). In this case, the total angular momentum \mathbf{J} is the vectorial sum of the end-over-end rotation \mathbf{N} and the total spin of the electrons \mathbf{S} ; for the $X^1\Sigma^+$ state, $\mathbf{J} = \mathbf{N}$. The expression for the unperturbed rotational energy is given by $B_\nu N(N+1)$. In the present study, the $b^3\Sigma^+$ state is merely used to enable parity- and rotational-level-selective detection of molecules in the $a^3\Pi$ state. The further splitting of the rotational levels due to the fine structure and hyperfine structure parts of the Hamiltonian, for which the explicit expressions are given elsewhere,²² is therefore not relevant and is not discussed here.

IV. ROTATIONALLY RESOLVED SPECTROSCOPY OF THE $a^3\Pi, \nu \leftarrow X^1\Sigma^+, \nu$ BANDS

Here, we present our spectroscopic investigation of the rotational structure of the metastable $a^3\Pi$ state up to $\nu = 7$. The spin-forbidden $a^3\Pi \leftarrow X^1\Sigma^+$ transition gets its intensity mainly from spin-orbit coupling of the $a^3\Pi$ state with a $^1\Pi$ state and, to a lesser extent, from spin-orbit coupling with a $^1\Sigma^+$ state.¹³ The $\Delta\Omega = 0$ selection rule for these couplings results in transitions to the $a^3\Pi_1$ manifold being the strongest, about a factor 20 stronger than those to the e levels of the $a^3\Pi_0$ manifold. Transitions to the $a^3\Pi_0, f$ levels and to the $a^3\Pi_2$ manifold are again about two orders of magnitude weaker. For more details on the spin-orbit coupling, see Sec. VI. Since the Franck-Condon matrix between the $a^3\Pi$ and $X^1\Sigma^+$ states is highly diagonal, only $\Delta\nu = 0$ bands are used in the experiments.

The characteristics of the TiSa-seeded PDA that is used for $a^3\Pi \leftarrow X^1\Sigma^+$ excitation are given in Sec. II. The setup, shown in Fig. 2, is arranged such that the $a^3\Pi \rightarrow X^1\Sigma^+$ phosphorescence is detected at $z = 65$ cm. This technique is used for a preliminary search of the energy levels of higher vibrational states of the $a^3\Pi$ state. In between excitation and phosphorescence detection, at $z = 45$ cm, a ToF-MS is installed for $(1 + 1')$ REMPI. This technique is more sensitive and allows for the accurate determination of selected rovibrational transition frequencies. The frequencies of the Q_2 and the $R_2(0)$ lines are measured for $\nu \leq 7$, and the transition frequencies of the $P_1(1)$ lines are measured for $\nu \leq 5$. The pulse energy of the PDA

(around 10 mJ) is sufficient to saturate the transitions to the $a^3\Pi_1$ manifold and to efficiently excite molecules to the e levels in the $a^3\Pi_0$ manifold. The signal intensity is mainly limited by the thermal population of the molecules in the initial vibrational level ν in the $X^1\Sigma^+$ ground state.

In Fig. 3, the measured Q_2 branches are shown for selected diagonal bands of the $a^3\Pi_1, \nu \leftarrow X^1\Sigma^+, \nu$ transition. It is evident from these spectra that the value for ΔB_ν , defined as the difference between the rotational constants in the $a^3\Pi, \nu$ and $X^1\Sigma^+, \nu$ states, increases with ν . The hyperfine structure cannot be resolved in these measurements and leads to a partial overlap of the $Q_2(1)$ and $Q_2(2)$ lines. The center frequency of the $Q_2(1)$ lines is determined from the measured center frequency of the spectrally isolated $R_2(0)$ lines, using the known rotational energy structure of the electronic ground

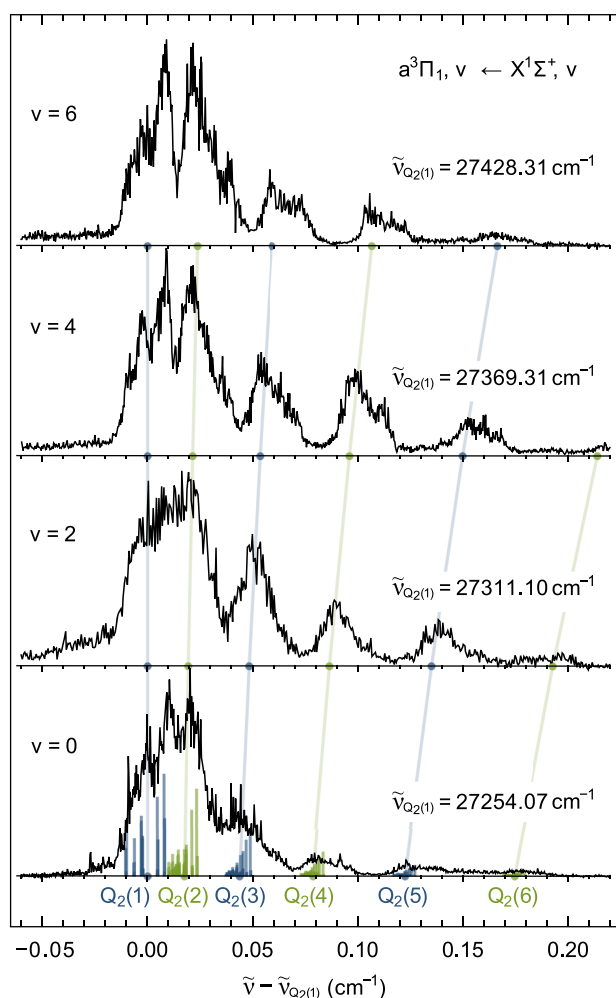


FIG. 3. Measured Q_2 lines of the $a^3\Pi_1, \nu \leftarrow X^1\Sigma^+, \nu$ bands for $\nu = 0, 2, 4,$ and 6 . The molecules in the metastable state are detected using two-color $(1 + 1')$ REMPI via the $b^3\Sigma^+, \nu$ state. The spectra are shifted such that the centers of the $Q_2(1)$ lines align. The calculated hyperfine structure of the Q_2 lines is given as a stick spectrum.

TABLE I. Fitted spectroscopic parameters for the $a^3\Pi$ state from this work, compared to the values reported earlier²⁷ and to the values for the $X^1\Sigma^+$ state.²⁴ All values are given in cm^{-1} .

Parameter	$a^3\Pi$, this work	$a^3\Pi$, Ref. 27	$X^1\Sigma^+$, Ref. 24
T_e	27 239.452 9(53)	27 239.4(1)	0
ω_e	830.280 7(11)	830.3(3)	802.324 47(11)
$\omega_e x_e$	4.643 64(58)	4.6(2)	4.849 915(44)
$\omega_e y_e$	0.012 30(12)	...	0.019 573 8(68)
$\omega_e z_e$	-0.000 111 9(78)	...	-0.000 034 07(35)
\tilde{A}_e	47.347 5(17)
$\tilde{\zeta}_e$	-0.073 91(28)
$\tilde{\eta}_e$	-0.000 695(48)
B_e	0.557 376(48)	0.557 18(3)	0.552 480 208(65)
α_e	0.004 798(30)	0.004 68(5)	0.004 984 261(44)
β_e	0.000 025 8(40)	...	0.000 017 215(95)

state.²⁴ The $Q_2(1)$ and $R_2(0)$ lines reach different parity components of the $a^3\Pi_1, J = 1$ level, but their splitting can be neglected (see Sec. VII). The spectra are shifted such that the centers of the $Q_2(1)$ lines are aligned at $\tilde{\nu} = 0$. The dots indicate the transition frequencies of the $Q_2(J)$ lines. The calculated hyperfine structure of the transitions to the $a^3\Pi_1, \nu = 0, J$ levels is given as a stick spectrum underneath, with their center of gravity aligned to the observed line centers. Note that the discrepancy that is evident between the line positions and the measured spectra is due to the side peak of the spectral profile of the PDA.

In total, 30 clearly separated lines are measured and their center frequencies are determined using Gaussian fits and listed in Table VII in Appendix A, together with the deviations between the measured and calculated frequencies. The spectroscopic parameters of the $a^3\Pi$ state deduced from a fit to all the measured frequencies are given in Table I. The standard deviation of the fit is about 40 MHz.

The effective electron spin-orbit coupling constant \tilde{A}_ν increases with ν , while the rotational constant B_ν decreases with ν . Using the expression for A_0 given in Eq. (4), we find a deviation of 11 MHz with the independently determined value.²² The value obtained for B_0 agrees to within 4 MHz with the value found earlier.¹³ The energy of the center of gravity of the $J = 1$ level in the $a^3\Pi_1, \nu = 0$ state relative to that of the $N = 0$ level in the $X^1\Sigma^+, \nu = 0$ state is consistent within 40 MHz to the value given earlier.²²

The experimentally derived spectroscopic constants are converted to an analytical potential using the least-square fitting procedure available through Le Roy's program.²⁸⁻³⁰ In particular, we obtain a reliable Rydberg-Klein-Rees (RKR) potential in a point-wise fashion utilizing the Dunham coefficients. This potential is then fitted to a given functional form through the betaFIT program of Le Roy and Pashov,²⁹ which in this case is the expanded Morse oscillator (EMO) potential function, as

$$V_{\text{EMO}}(r) = D_e \left(1 - e^{-\beta(r)(r-r_e)} \right)^2, \quad (8)$$

where r_e represents the equilibrium distance, D_e is the dissociation energy, and

TABLE II. Parameters of the empirical EMO potential for the $a^3\Pi$ state of AlF. The dissociation energy and the equilibrium distance are kept fixed at $D_e = 28\,324.6$ cm^{-1} and $r_e = 1.647\,08$ Å. The dimensionless root mean square deviation is 0.58. All values are in Å $^{-1}$.

$\beta_0 = 1.995\,686(69)$	$\beta_3 = -21.6(4.3)$	$\beta_6 = 1006(210)$
$\beta_1 = 0.086\,3(43)$	$\beta_4 = 233(43)$	
$\beta_2 = 0.26(12)$	$\beta_5 = -815(160)$	

$$\beta(r) = \sum_{i=0}^{N_\beta} \beta_i [y_{\text{ref}}^q(r)]^i. \quad (9)$$

Here, N_β accounts for the number of anharmonic terms included in the potential and

$$y_{\text{ref}}^q(r) = \frac{r^q - r_{\text{ref}}^q}{r^q + r_{\text{ref}}^q} \quad (10)$$

represents a normalized interatomic distance designed to enhance the precision of the fitting procedure. The results of the fitting procedure for the $a^3\Pi$ state of AlF are summarized in Table II. In the fit, the reference distance $r_{\text{ref}} = 1.45$ Å and $q = 2$ are used to fit the point-wise RKR potential into an EMO potential. The equilibrium distance r_e and the dissociation energy D_e are maintained as fixed parameters. The last one is calculated using the results of this study, combined with the recent and most accurate measurement of the dissociation energy of the $X^1\Sigma^+$ state.¹⁶

V. AC STARK SHIFTS ON THE $a^3\Pi_0, v = 4 \leftarrow X^1\Sigma^+, v = 4$ BAND

While recording the $P_1(1)$ line of the $a^3\Pi_0, v = 4 \leftarrow X^1\Sigma^+, v = 4$ band, we noted that the expected 220 MHz wide single line is asymmetrically shaped. The line is broadened to about 500 MHz and shaded to lower frequencies such that the center frequency appears about 200 MHz lower than anticipated. For that reason, this line is left out of the fitting of the spectroscopic parameters of the $a^3\Pi$ state and is not listed in Table VII. Other rotational lines of the same band show distorted, asymmetric line shapes as well, broadened significantly beyond the expected span of the hyperfine structure. As explained in the following, these observations are well accounted for by AC Stark shifts due to near-resonant rotational lines of the much more intense $c^3\Sigma^+, v = 3 \leftarrow a^3\Pi_0, v = 4$ band.

In order to efficiently induce the weak transitions from the $X^1\Sigma^+$ state to the $a^3\Pi_0$ manifold, laser pulses of about 10 mJ energy, 5 ns duration, and with a bandwidth of 220 MHz are used. The approximately circular collimated beam has a diameter of several mm. In the presence of other strong transitions that are coincidentally nearby and involve the same J level in the $a^3\Pi_0$ state, the high electric field $\mathcal{E}(\tilde{\nu}_i)$ associated with the laser pulse at frequency $\tilde{\nu}_i$ causes a shift of this J level. The magnitude of the energy shift, $\delta E(J)$, is given by³¹

$$\delta E(J) \propto \sum_i \frac{|\mu_i \mathcal{E}(\tilde{\nu}_i)|^2}{h(\tilde{\nu}_i - \tilde{\nu}_i)}, \quad (11)$$

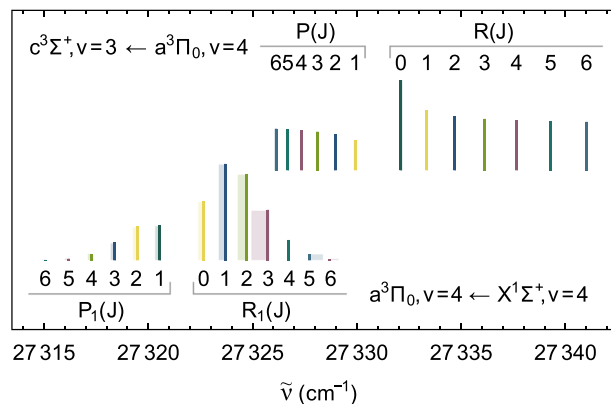


FIG. 4. Calculated line positions of the $a^3\Pi_0, v = 4 \leftarrow X^1\Sigma^+, v = 4$ and $c^3\Sigma^+, v = 3 \leftarrow a^3\Pi_0, v = 4$ bands. Transitions that have a J level in the $a^3\Pi_0, v = 4$ state in common have the same color. The heights of the lines in the upper spectrum reflect the Hönl-London factors, whereas in the lower spectrum, these reflect the expected line intensities for $T_{\text{rot}} = 5$ K. The expected (relative) magnitude and sign of the AC Stark shift are indicated by the shaded boxes in the lower spectrum.

with the transition frequencies $\tilde{\nu}_i$, the transition dipole moments μ_i , and the Planck's constant h . It is evident from Eq. (11) that only levels with $\tilde{\nu}_i \approx \tilde{\nu}_i$ contribute significantly to the total shift $\delta E(J)$.

The origin of the $a^3\Pi_0, v = 4 \leftarrow X^1\Sigma^+, v = 4$ band is about 10 cm^{-1} below the origin of the $c^3\Sigma^+, v = 3 \leftarrow a^3\Pi_0, v = 4$ band, as schematically shown in Fig. 4. The latter transition is spin-allowed, and even though $\Delta v = -1$, the transition dipole moment is estimated to be about three orders of magnitude larger than for the spin-forbidden $a^3\Pi_0, v = 4 \leftarrow X^1\Sigma^+, v = 4$ transition. When the laser is tuned to resonance with the $P_1(1)$ line of the $a^3\Pi_0, v = 4 \leftarrow X^1\Sigma^+, v = 4$ band, the near-resonance of the laser frequency with the $R(0)$ transition of the $c^3\Sigma^+, v = 3 \leftarrow a^3\Pi_0, v = 4$ band shifts the $J = 0$ level in the $a^3\Pi_0, v = 4$ to lower energy. For levels with $J > 0$ in the $a^3\Pi_0, v = 4$ state, both the $P(J)$ and the $R(J)$ lines of the $c^3\Sigma^+, v = 3 \leftarrow a^3\Pi_0, v = 4$ band contribute to its overall shift. In Fig. 4, transitions that have a J level in the $a^3\Pi_0, v = 4$ state in common are indicated by the same color. Their relative contribution scales with the normalized Hönl-London factor for a $a^3\Sigma^+ \leftarrow a^3\Pi_0$ transition, indicated in Fig. 4 by the height of the lines in the $c^3\Sigma^+, v = 3 \leftarrow a^3\Pi_0, v = 4$ spectrum. The frequency shift $\delta\tilde{\nu}(J)$ expected for the $P_1(J+1)$ or $R_1(J-1)$ lines of the $a^3\Pi_0, v = 4 \leftarrow X^1\Sigma^+, v = 4$ band that reach the level J in the $a^3\Pi_0, v = 4$ state is given by

$$\delta\tilde{\nu}(J) \propto \frac{I}{2J+1} \left(\frac{J}{\tilde{\nu} - \tilde{\nu}_{P(J)}} + \frac{J+1}{\tilde{\nu} - \tilde{\nu}_{R(J)}} \right). \quad (12)$$

Here, I is the intensity of the laser at the (unperturbed) frequency $\tilde{\nu}$ for the $P_1(J+1)$ or $R_1(J-1)$ lines of the $a^3\Pi_0, v = 4 \leftarrow X^1\Sigma^+, v = 4$ band, respectively. The frequencies $\tilde{\nu}_{P(J)}$ and $\tilde{\nu}_{R(J)}$ are those of the $P(J)$ and $R(J)$ lines of the $c^3\Sigma^+, v = 3 \leftarrow a^3\Pi_0, v = 4$ band, i.e., from $a^3\Pi_0, v = 4, J$ to $c^3\Sigma^+, v = 3, N = J-1$ and $c^3\Sigma^+, v = 3, N = J+1$, respectively.

In the experiment, the AlF molecules in the beam interact with the pulsed radiation of the PDA and experience an intensity that varies over time. In addition, as the molecules can be considered

stationary, while they interact with the laser pulse, they experience an intensity that depends on their position in the laser beam. This explains why we do not observe an overall spectral shift of the $P_1(1)$ line, but rather an asymmetric broadening and shading toward lower frequencies. The temporal and spatial profile of the laser beam is the same throughout the spectral range of the $a^3\Pi_0, \nu = 4 \leftarrow X^1\Sigma^+, \nu = 4$ band, and its effect as imprinted in the spectral shape of the $P_1(1)$ line can be used to model all the other lines in the spectrum. The $P_1(1)$ line is particularly suited for this because it only experiences an AC Stark shift due to the $R(0)$ line of the $c^3\Sigma^+, \nu = 3 \leftarrow a^3\Pi_0, \nu = 4$ band, and as mentioned earlier, the $P_1(1)$ line is intrinsically very narrow.

To model the other $P_1(J+1)$ and $R_1(J-1)$ lines of the $a^3\Pi_0, \nu = 4 \leftarrow X^1\Sigma^+, \nu = 4$ band that reach levels with $J > 0$ in the $a^3\Pi_0, \nu = 4$ state, we take the observed spectral structure of the $P_1(1)$ line, stretched on the frequency axis with the calculated ratio of $\delta\tilde{\nu}(J)/\delta\tilde{\nu}(0)$. In the stick spectrum in Fig. 4, as well as for the measured lines in Fig. 5, this ratio is indicated by the shaded area. The calculated ratio $\delta\tilde{\nu}(J)/\delta\tilde{\nu}(0)$ decreases for increasing values of J in the P_1 branch, whereas in the R_1 branch, it increases from $J = 1$ to $J = 4$, peaks for $J = 5$, and changes sign at $J = 6$ and decreases again for increasing J .

The large value at $J = 5$ is due to the very near coincidence of the $R_1(4)$ line of the $a^3\Pi_0, \nu = 4 \leftarrow X^1\Sigma^+, \nu = 4$ band with the $P(5)$ line of the $c^3\Sigma^+, \nu = 3 \leftarrow a^3\Pi_0, \nu = 4$ band, broadening the $R_1(4)$ line to an extent such that we have not observed it. Levels with $J > 0$ in the $a^3\Pi_0, \nu = 4$ state have an additional contribution to the width of the observed spectral lines due to the hyperfine structure in the $a^3\Pi_0, \nu = 4$ state that spans approximately $J \cdot 200$ MHz. This simple model represents the observed spectral shapes very well, as is shown for the six rotational lines in Fig. 5.

The origin of the $C^1\Sigma^+, \nu = 0 \leftarrow a^3\Pi_0, \nu = 4$ band is only about 1.5 cm^{-1} below the origin of the $a^3\Pi_0, \nu = 4 \leftarrow X^1\Sigma^+, \nu = 4$ band. The transition dipole moment of this spin-forbidden, $\Delta\nu = -4$, band is very small, and it is not expected to cause a visible AC Stark shift of the levels in the $a^3\Pi_0, \nu = 4$ state; the magnitude and direction of the shading of the spectral lines would be quite different from the observed one. There is an accidental overlap ($<0.10 \text{ cm}^{-1}$) between the $R_1(0)$ line of the $a^3\Pi_0, \nu = 4 \leftarrow X^1\Sigma^+, \nu = 4$ band and the $R(1)$ line of the $C^1\Sigma^+, \nu = 0 \leftarrow a^3\Pi_0, \nu = 4$ band. This overlap probably causes the $S(0)$ two-photon transition from the $X^1\Sigma^+, \nu = 4, N = 0$ level to the $C^1\Sigma^+, \nu = 0, N = 2$ level, followed by one-photon ionization, to be quite strong and likely explains why the $R_1(0)$ line of the $a^3\Pi_0, \nu = 4 \leftarrow X^1\Sigma^+, \nu = 4$ band (shown in Fig. 5) is considerably weaker than expected.

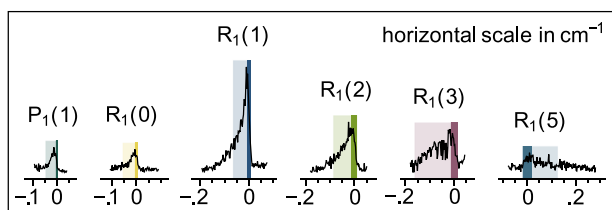


FIG. 5. Measured line shapes together with their expected shading. The widths of the solid vertical bars are the spans of the hyperfine structure of the transitions.

VI. RADIATIVE LIFETIMES IN THE $a^3\Pi, \nu = 0$ STATE

As mentioned before, the $a^3\Pi \leftarrow X^1\Sigma^+$ transition becomes weakly allowed due to spin-orbit coupling of the $a^3\Pi$ state with a $^1\Pi$ state and, to a lesser extent, with a $^1\Sigma^+$ state. The $\Delta\Omega = 0$ selection rule for these couplings makes transitions to the $a^3\Pi_1$ manifold about a factor 20 stronger than those to the $a^3\Pi_0$ manifold. Both the e and f levels of the $a^3\Pi_1$ manifold can be reached from the $X^1\Sigma^+$ state, and the transitions to the lowest J levels are the strongest. As only the e levels of the $a^3\Pi_0$ manifold can interact with a $^1\Sigma^+$ state, only these can be reached from the electronic ground state for low values of J . For higher values of J , the $\Omega = 1$ character in the wavefunctions of the levels in the $a^3\Pi_2$ and $a^3\Pi_0$ manifolds increases; see Table IX. Consequently, transitions from the electronic ground state to higher rotational levels become gradually more allowed. The spin-orbit coupling mechanism makes the lifetimes of the rotational levels in the $a^3\Pi$ state strongly Ω -, J -, and e/f -dependent.²⁰ The lifetime of the $a^3\Pi_1, J = 1$ level is the shortest. The low- J , e , and f levels of the $a^3\Pi_2$ manifold and the low- J , f levels of the $a^3\Pi_0$ manifold live up to three orders of magnitude longer; the $a^3\Pi_0, J = 0, f$ level cannot decay to the electronic ground state via an electric dipole allowed transition (see Appendix B, Table X).

Measuring the lifetime of metastable states of molecules is challenging, as neutral molecules can generally not be kept long enough in the observation volume. As discussed above, the lifetimes of electronically excited, metastable states generally strongly depend on the exact (rotational) quantum level, requiring state-selective preparation or detection techniques. An accurate measurement of the radiative lifetime of selected rotational levels of CO in the $a^3\Pi, \nu = 0$ state could only be performed when these molecules were state-selectively prepared and subsequently decelerated and electrostatically trapped.³² The thus determined lifetime is in excellent agreement with the result of a recent relativistic, *ab initio* calculation.³³ Prior to these measurements with trapped CO molecules, the most accurate results were obtained from molecular beam experiments, employing two spatially separated LIF detection zones.³⁴ These experiments determined a lifetime that is 30% too large, exemplifying the inherent challenges of such measurements. For the here presented lifetime measurement of the $a^3\Pi, \nu = 0$ state of AlF, we use an improved method that reduces systematic errors. In this method, the signal from the molecules in the $\Omega = 1$ manifold is calibrated against that of the molecules in the $\Omega = 0$ manifold.

The molecules are excited either on the $R_2(0)$ or on the $R_1(0)$ line to the $J = 1, e$ level of the $a^3\Pi_1, \nu = 0$ or $a^3\Pi_0, \nu = 0$ manifold. The measured, spectrally integrated intensities of these two lines are given by $I_{R_2(0)}$ and $I_{R_1(0)}$. We state-selectively detect the population in the metastable state in two spatially separated ToF mass spectrometers and measure the ratio of the two ion signals as a function of the time-of-flight T between the two detection regions. The value of T is varied by using different carrier gases and by changing the distance between the two mass spectrometers. The first detection zone (A) is mounted at $z_A = z_{\text{PDA}} + 5.5 \text{ cm}$, and the second one (B) either at $z_{B,1} = z_{\text{PDA}} + 47.0 \text{ cm}$ or at $z_{B,2} = z_{\text{PDA}} + 97.0 \text{ cm}$. The population in the $a^3\Pi_{\Omega}, \nu = 0, J = 1, e$ level at $z = z_A$ is referred to as $N_{\Omega,A}(T = 0)$, and the measured ion signal is referred to as $S_{\Omega,A}(T = 0)$. The population in this same level at $z = z_B$ is referred to as $N_{\Omega,B}(T)$ and the corresponding signal intensity as $S_{\Omega,B}(T)$. The lifetime of the $a^3\Pi_{\Omega}, \nu = 0, J = 1, e$ level is labeled τ_{Ω} . Using these expressions, for

the ratio of the ion signals measured in the two detection zones, we get

$$\frac{S_{\Omega,B}(T)}{S_{\Omega,A}(T=0)} = \frac{\alpha_{\Omega,B}}{\alpha_{\Omega,A}} \frac{N_{\Omega,B}(T)}{N_{\Omega,A}(T=0)} = \frac{\alpha_{\Omega,B}}{\alpha_{\Omega,A}} e^{-T/\tau_{\Omega}}, \quad (13)$$

with $\alpha_{\Omega,A}$ and $\alpha_{\Omega,B}$ being the detection efficiencies of zones (A) and (B). When the PDA and the ionization laser are aligned in the same way throughout the whole measurement, we can assume that $\alpha_{0,B}/\alpha_{0,A} = \alpha_{1,B}/\alpha_{1,A}$. Then, the “ratio-of-ratios” $\mathcal{R}(T)$ is given by

$$\mathcal{R}(T) = \frac{S_{1,B}(T)}{S_{1,A}(T=0)} \bigg/ \frac{S_{0,B}(T)}{S_{0,A}(T=0)} = e^{-T/\tau_{\text{exp}}}, \quad (14)$$

where

$$\frac{1}{\tau_{\text{exp}}} = \frac{1}{\tau_1} - \frac{1}{\tau_0}. \quad (15)$$

To determine the absolute values of τ_1 and τ_0 from τ_{exp} , the ratio of τ_1 and τ_0 needs to be known. The latter can be deduced from $I_{R_2(0)}/I_{R_1(0)}$.

In the experiment, the vertical spread of the molecular beam is confined by a 2 mm slit, placed just in front of the intersection with the 367 nm laser. The size of the PDA preparation beam is constrained by an iris aperture, transmitting 3 mJ of pulse energy in a 3 mm diameter beam. AIF is ionized using (1 + 2) REMPI via the $b^3\Sigma^+$ state. The ionization laser beam is defined with 10 mm diameter apertures to avoid striking the ToF electrodes. This laser passes first through zone (B) and then through zone (A); the pulse energy is about 7 mJ in zone (B) and 5 mJ in zone (A). The alignment of the ionization laser stays the same throughout; switching between the two detection regions is achieved by changing the timing of the laser pulse. The values for the “ratio-of-ratios” $\mathcal{R}(T)$ are recorded as a function of T by using helium, neon, argon, krypton, and xenon as carrier gases and the two different ToF-positions $z_{B,1}$ and $z_{B,2}$. The results of the measurements are shown in Fig. 6. The error bars show the standard deviation from a series of measurements for every data point. An exponential function according to Eq. (14) fitted to the data yields a value of $\tau_{\text{exp}} = 2.04 \pm 0.16$ ms.

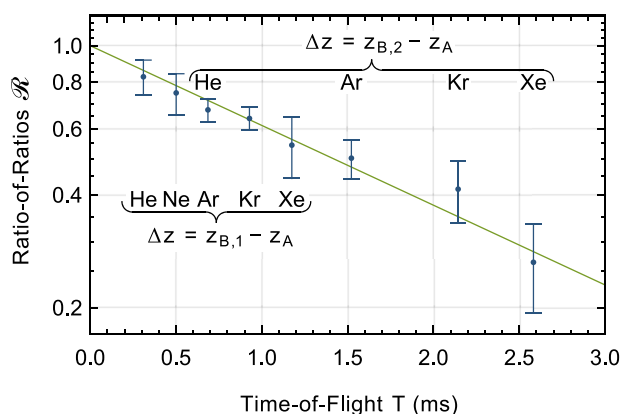


FIG. 6. Measured values for the “ratio-of-ratios” $\mathcal{R}(T)$ as a function of the time-of-flight T , shown on a semi-log plot. A fit to the data gives the characteristic lifetime $\tau_{\text{exp}} = 2.04 \pm 0.16$ ms.

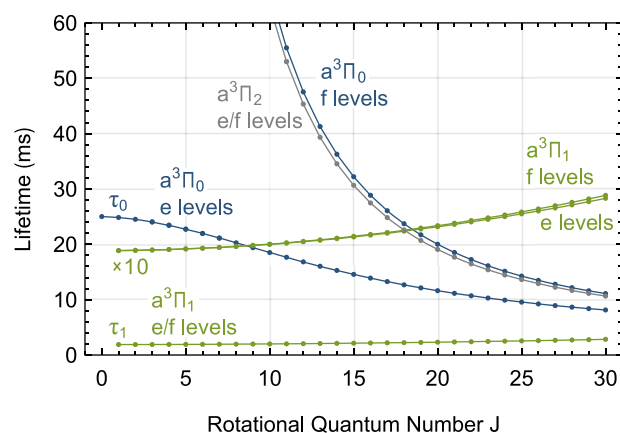


FIG. 7. Calculated lifetimes of the rotational levels in the $a^3\Pi, \nu = 0$ state of AIF. The absolute scale is set by the lifetime of the $a^3\Pi_1, \nu = 0, J = 1, e$ level, experimentally determined as $\tau_1 = 1.89 \pm 0.15$ ms. The lifetimes of the rotational levels in the $\Omega = 1$ manifold are also shown on an expanded ($\times 10$) scale.

The intensity ratio $I_{R_2(0)}/I_{R_1(0)}$ is measured as 20.9 ± 1.0 . The different intensities of these lines are due to the different degree of coupling of the $a^3\Pi_{\Omega}, \nu = 0, J = 1, e$ levels to the $X^1\Sigma^+, \nu = 0, N = 0$ level. This coupling is due to transition dipole moments obtained from mixing with pure singlet states, either $^1\Pi$ or $^1\Sigma^+$ states. These separate contributions can either interfere constructively or destructively. The observation that the P_1 lines are considerably weaker than the R_1 lines¹³ is only consistent with the case of destructive interference. From the analysis given in Appendix B, it is derived that for destructive interference, $\tau_0/\tau_1 = 13.1 \pm 1.1$. From this, we conclude that the lifetime of the $a^3\Pi_1, \nu = 0, J = 1, e$ level is $\tau_1 = 1.89 \pm 0.15$ ms and the lifetime of the $a^3\Pi_0, \nu = 0, J = 1, e$ level is $\tau_0 = 24.8 \pm 2.9$ ms.

In Fig. 7, the calculated lifetimes for the rotational levels in the $a^3\Pi, \nu = 0$ state of AIF are shown. For several of the lowest J levels, these lifetimes are listed in Table X. These values are calculated using the known spectroscopic constants in the $a^3\Pi, \nu = 0$ state, assuming that the lifetimes are solely determined by electric dipole allowed transitions and taking both the J -dependent $^1\Pi$ and $^1\Sigma^+$ character of the wavefunctions in the $a^3\Pi, \nu = 0$ state into account.

VII. HYPERFINE STRUCTURE IN THE $a^3\Pi, \nu = 5$ STATE

The hyperfine structure results from the interaction of the nuclear spins of the aluminum and fluorine atoms with the electronic and rotational degrees of freedom and is described by the term H_{hfs} in the molecular Hamiltonian, Eq. (1). The vectorial coupling of the rotational angular momentum J with the spins of the aluminum nucleus I_{Al} and the fluorine nucleus I_{F} leads to the final vector F , i.e., $F = J + I_{\text{Al}} + I_{\text{F}}$.

Here, we present our investigation of the hyperfine structure of the $a^3\Pi_1, \nu = 5$ state. We measure all 26 allowed radio frequency transitions between F levels of opposite parity within the $J = 1$ level and a few transitions in the $J = 2$ level. To measure the transitions in the $J = 1$ level, the molecules are prepared with the PDA on the $R_2(0)$ or $Q_2(1)$ line in the six, definite parity F levels. The metastable

molecules subsequently pass through an rf transmission line centered at $z_{\text{rf}} = z_{\text{PDA}} + 10$ cm, where they are exposed to rf radiation in the 1–500 MHz range that propagates perpendicular to the direction of the molecular beam. Since the population in the $X^1\Sigma^+, \nu = 5$ state is about two orders of magnitude less than that in the vibrational ground state, a relatively short transmission line of 57 mm is used in order to be able to record spectral lines with a high enough signal-to-noise ratio.

The ambient magnetic field in the rf interaction region is about 20 μT . The exact timing and duration of the rf pulse are controlled by an rf switch. When the rf radiation is tuned to an electric dipole allowed transition, the population is transferred to an F level with opposite parity. Given the many M_F sublevels involved in the transitions and the presence of a weak magnetic field, it is not possible to apply a perfect π pulse, and the duration and power of the applied rf radiation are thereby merely adjusted to maximize the total population transfer. After exiting the rf interaction region, the molecules enter the detection region, where parity-selective excitation to the $b^3\Sigma^+, \nu = 5$ state followed by ionization takes place in a two-color ($1 + 1'$) REMPI process. By recording the parent ion signal while scanning the frequency of the rf radiation, background-free rf spectra are obtained.

The widths of the observed rf spectral lines are mainly determined by Zeeman broadening due to the ambient magnetic field.

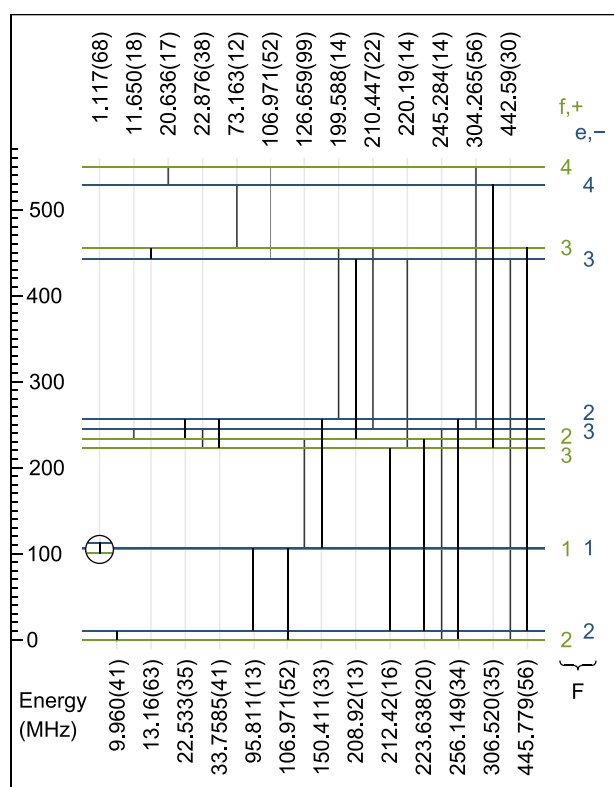


FIG. 8. Hyperfine energy level diagram of the $J = 1$ level in the $a^3\Pi_1, \nu = 5$ state. All 26 allowed rf transitions are indicated with their measured frequencies and error bars (in MHz). The quantum numbers F and the parities of the levels are given.

Depending on the difference of the Landé g_F factors of the coupled levels, the full widths at half maximum range typically from 40 to 200 kHz. The center frequency and width of in total 41 hyperfine transitions are determined with Gaussian fits. The measured frequencies for the 26 possible transitions within the $J = 1$ level and their assignments in the energy level scheme are given in Fig. 8, together with the measured error bars. All measured frequencies are fitted to the Hamiltonian, and the obtained hyperfine structure parameters are given in Table III. In the fit, several hyperfine parameters are kept fixed at the values found for the $\nu = 0$ state. The values for the spin-orbit coupling constant and for the rotational constant of $\nu = 5$ are taken from Sec. IV and are also kept fixed in this fit. The standard deviation of the fit is 20 kHz. As expected, the overall structure of the hyperfine levels in $\nu = 5$ is very similar to that in $\nu = 0$.

For a comparison of these hyperfine parameters to theory, the electric field gradients (EFGs), and the nuclear quadrupole coupling constant eq_0Q , the isotropic Fermi contact coupling constants b_F and the anisotropic spin dipole coupling constants c and d are calculated by the density functional theory (DFT) method implemented in Gaussian 2016.³⁵ The hybrid exchange–correlation functional

TABLE III. Λ -doubling parameter q and hyperfine structure parameters for the $a^3\Pi_1, \nu = 5$ state obtained from the best fit to the experimental data together with the product of the standard deviation and \sqrt{Q} (all values are in MHz). These values are compared with those determined earlier for the $a^3\Pi_1, \nu = 0$ state. For $\nu = 0$, the parameters $A_0 = 1\,420\,870$ MHz and $\lambda_0 = 2659$ MHz are kept fixed,¹³ whereas for $\nu = 5$, $A_5 = 1\,431\,589$ MHz and $\lambda_5 = 2766$ MHz are used.²²

Parameter	Value (MHz) $\nu = 0$	SD $\cdot \sqrt{Q}$ $\nu = 0$	Value (MHz) $\nu = 5$	SD $\cdot \sqrt{Q}$ $\nu = 5$
B	16 634.7	0.0010	15 942.1	fixed
γ	-7.6089	0.0526	-7.6089	fixed
o	4 968.32	0.0510	4 968.32	fixed
$o^{(R)}$	-0.0061	0.0012	-0.0061	fixed
p	-24.3462	0.0510	-24.3462	fixed
q	-1.8176	0.0023	-1.9192	0.0009
$a(\text{Al})$	199.162	0.0353	200.2192	0.1339
$b_F(\text{Al})$	1 247.97	0.2783	1 215.9123	2.9445
$b_F^{(R)}(\text{Al})$	0.0222	0.0045	0.0222	fixed
$c(\text{Al})$	-21.0093	0.4124	-21.0093	fixed
$c^{(R)}(\text{Al})$	-0.0568	0.0114	-0.0568	fixed
$d(\text{Al})$	121.908	0.0155	124.1718	0.0604
$eq_0Q(\text{Al})$	-12.9921	0.0159	-10.8595	0.0811
$eq_0Q_{LS}(\text{Al})$	-0.039 2	0.0042	-0.0392	fixed
$eq_2Q(\text{Al})$	51.1137	0.0054	51.8014	0.0220
$C_I(\text{Al})$	-0.0569	0.0169	-0.0569	fixed
$C_I'(\text{Al})$	-0.0115	0.0007	-0.0115	fixed
$a(\text{F})$	207.135	0.0109	197.2087	0.4804
$a^{(R)}(\text{F})$	-0.0688	0.0038	-0.0688	fixed
$b_F(\text{F})$	169.629	0.1605	146.1175	10.9697
$b_F^{(R)}(\text{F})$	-0.0346	0.0019	-0.0346	fixed
$c(\text{F})$	122.804	0.2596	122.804	fixed
$d(\text{F})$	119.277	0.0868	112.8507	0.3054
$C_I'(\text{F})$	0.0346	0.0041	0.0346	fixed

TABLE IV. Spectroscopic parameters of AlF, including the term value T_e , the equilibrium internuclear distance r_e , and the harmonic frequency ω_e at the CAM-B3LYP/aug-cc-pV5Z level.

State	T_e (cm ⁻¹)	r_e (Å)	ω_e (cm ⁻¹)
X ¹ Σ ⁺	0	1.659	792.87
a ³ Π	25 587.86	1.655	818.72

TABLE V. The DFT-calculated hyperfine constants $eq_0Q(\text{Al})$, $b_F(\text{Al})$, $b_F(\text{F})$, $c(\text{Al})$, $c(\text{F})$, $d(\text{Al})$, and $d(\text{F})$ (in MHz) of the a³Π state of AlF for different vibrational levels.

ν	$eq_0Q(\text{Al})$	$b_F(\text{Al})$	$b_F(\text{F})$	$c(\text{Al})$	$c(\text{F})$	$d(\text{Al})$	$d(\text{F})$
0	-12.221	1186.2	150.1	-24.6	154.3	126.5	128.6
1	-11.763	1189.8	147.0	-25.3	160.8	126.9	127.1
2	-11.309	1193.1	144.0	-25.9	167.6	127.4	125.5
3	-10.857	1196.2	141.0	-26.6	174.7	127.8	124.0
4	-10.407	1199.1	138.0	-27.2	182.0	128.3	122.4
5	-9.957	1201.7	135.1	-27.9	189.7	128.7	120.8

CAM-B3LYP³⁶ with an aug-cc-pV5Z basis set³⁷⁻³⁹ is used for the a³Π state of AlF. To obtain these constants, we calculate the interaction potential of AlF for 23 points ranging from 1.0 to 6.0 Å. The nuclear quadrupole coupling constant eq_0Q (in MHz) is calculated from its relationship between the EFGs (in atomic units) and the nuclear quadrupole moment Q (in MBarn) as^{40,41}

$$eq_0Q = \frac{Q\langle V_{zz} \rangle_\nu}{4.255\,958}, \quad (16)$$

where $Q = 146.6$ Mb for the ²⁷Al atom⁴² and $\langle V_{zz} \rangle_\nu = \langle \psi_\nu | V_{zz} | \psi_\nu \rangle$ stands for the expectation value of V_{zz} for a given vibrational state $|\psi_\nu\rangle$. Bound vibrational states are calculated using a discrete variable representation (DVR) approach^{43,44} employing 200 DVR points, whereas the interaction potential is fitted to the DFT potential energy curve, characterized by the values given in Table IV. The resulting hyperfine constants are summarized in Table V. Note that the hyperfine parameter a is not listed. Often, the expression $a = d + c/3$ is used to deduce the value of a .⁴⁵ However, it is clear from the experimentally determined parameters listed in Table III that this expression does not hold for the a³Π state of AlF.

VIII. ABSENCE OF LIFETIME BROADENING IN rf SPECTRA OF THE a³Π₁, $\nu = 0$ STATE

Spectral lines with subnatural linewidths can be measured when one selectively probes those atoms or molecules that have stayed in the excited state longer than their natural lifetime.⁴⁶ More interestingly, when both levels involved in the transition are metastable and have the same lifetime, no additional broadening of the Rabi line shape due to the finite lifetime of the levels is expected at all in a time-resolved measurement.⁴⁷ The latter can be tested already for interaction times that are shorter than the lifetime, provided that the Rabi line shape is recorded with a sufficient accuracy. To explicitly demonstrate this, we record the $F = 4, + \leftarrow F = 4, -$ transition within the a³Π₁, $\nu = 0, J = 1$ level with an rf interaction time that is about

one third of the lifetime. For this, a parallel plate transmission line of 30 cm length is used. The electric field propagates along the molecular beam with amplitude \mathcal{E}_0 . Using xenon as a carrier gas, the total interaction time of the molecules with the rf radiation field is 650 μs. The rf interaction region is shielded by a μ-metal cylinder, resulting in an ambient magnetic field of <3 μT that is predominantly parallel to the electric field. The value of \mathcal{E}_0 is experimentally set such that the population transfer is optimized. The molecules in the $F = 4, +$ level are state-selectively detected shortly after exiting the rf interaction zone using (1 + 2) REMPI. The measured ion signal as a function of the rf frequency f is shown in Fig. 9.

The calculated Rabi line shape $\mathcal{R}(f)$ contains the eight possible $\Delta M_F = 0$ components. The ambient magnetic field splits these eight components apart. The Landé g_F factors for the upper and lower level are almost identical, with $\Delta g_F = 1.1 \cdot 10^{-4}$. As a result, the outermost components are separated by about 36 Hz. Transitions with $\Delta M_F = \pm 1$ are shifted by ±4.7 kHz but are not observed due to the near parallel orientation of the electric and magnetic fields. The green curve in Fig. 9 shows a fit of $\mathcal{R}(f)$ to the experimental data with the amplitude, central frequency, and value of $M_F\mu\mathcal{E}_0$ as free fit parameters. Here, μ is the effective transition dipole moment for the $M_F = 1 \leftarrow M_F = 1$ transition. The fitted FWHM of the Rabi line shape is 1.27 kHz.

To confirm that we, indeed, do not observe any broadening due to the finite lifetime of the two levels involved, we fit a convolution of the Rabi line shape with a Lorentzian $\mathcal{L}(f)$. This line shape is shown as the blue curve in Fig. 9. As the lifetime τ_1 of both coupled levels is 1.89 ms (see Table X), the natural width of the Lorentzian that would be observed in a stationary measurement is given by $(\pi\tau_1)^{-1}$ as 168 Hz, shown as the gray curve in Fig. 9. The pure Rabi line shape fits the experimental data best. In particular, the minima of the experimental signal next to the central peak are systematically described better when no broadening due to the lifetime of the metastable levels is included.

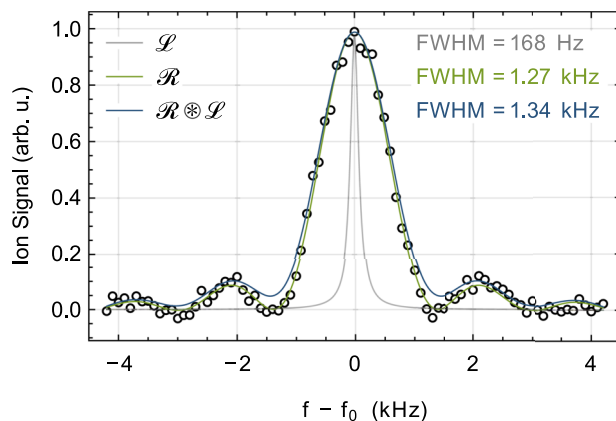


FIG. 9. Line shape of the $F = 4, + \leftarrow F = 4, -$ transition within the a³Π₁, $\nu = 0, J = 1$ level at $f_0 = 21.826\,40$ MHz. The circles are the experimental values. The gray curve shows a Lorentzian profile $\mathcal{L}(f)$ with a linewidth of $(\pi\tau_1)^{-1}$. The green and blue curves show a Rabi line shape $\mathcal{R}(f)$ and a convolution of the Rabi line shape with the Lorentzian $\mathcal{R}(f) \otimes \mathcal{L}(f)$.

IX. CONCLUSIONS AND OUTLOOK

This paper reports on the spectroscopic characterization of the $a^3\Pi$ state of AlF using a jet-cooled, pulsed molecular beam machine. The rovibrational constants determined in this work for the $a^3\Pi$ state enable the construction of an accurate electronic potential. Together with the best known potential for the $X^1\Sigma^+$ state, this is used to calculate the Franck–Condon factors for the $a^3\Pi$ – $X^1\Sigma^+$ system, as given in Table VI. The system is highly diagonal, and the transitions from the $a^3\Pi, \nu = 0$ state to the $X^1\Sigma^+, \nu = 1$ and $\nu = 2$ states are more than two and almost five orders of magnitude weaker than those to the $\nu = 0$ state.

The lifetimes of the rotational levels in the $a^3\Pi$ state of AlF strongly depend on the Ω manifold and on their e/f character. From the $N = 1$ level in the $X^1\Sigma^+, \nu = 0$ state, rotationally closed transitions can be induced to (i) the $J = 1, f$ level in the $A^1\Pi, \nu = 0$ state, (ii) the $J = 1, f$ level in the $a^3\Pi_1, \nu = 0$ state and the $J = 1, f$ level in the $a^3\Pi_0, \nu = 0$ state, and (iii) the $J = 0, e$ level in the $a^3\Pi_0, \nu = 0$ state. All these transitions are vibrationally closed to better than 99.2%, and the lifetimes of the upper levels vary from 1.9 ns ($J = 1, f$ in $A^1\Pi$) via 1.89 ms ($J = 1, f$ in $a^3\Pi_1$) and 25 ms ($J = 0, e$ in $a^3\Pi_0$) to 3.4 s ($J = 1, f$ in $a^3\Pi_0$). The latter value is calculated from the fraction of $\Omega = 1$ character in the wavefunction of the $J = 1, f$ level in $a^3\Pi_0$ and the measured lifetime of the $J = 1, f$ level in $a^3\Pi_1$.

The information on the Franck–Condon matrix and the lifetime of the rotational levels of the $a^3\Pi$ – $X^1\Sigma^+$ system obtained here is crucial for future laser cooling experiments. The duration that molecules stay in a certain rotational level in the $a^3\Pi, \nu = 0$ state can be made considerably shorter than their lifetime by driving the $A^1\Pi, \nu = 0 \leftarrow a^3\Pi, \nu = 0$ transition. From the $A^1\Pi, \nu = 0$ state, the molecules decay rapidly to the ground state. In this way, the scattering rate on the narrow $a^3\Pi, \nu = 0 \leftarrow X^1\Sigma^+, \nu = 0$ transition can be increased. Four transitions are required to return to the initial $N = 1$ rotational level in the $X^1\Sigma^+, \nu = 0$ state: (i) excitation on the $P_1(1)$ line of the $a^3\Pi_0, \nu = 0 \leftarrow X^1\Sigma^+, \nu = 0$ band, (ii) rf transitions from the e to the f levels in the $a^3\Pi_0, \nu = 0, J = 0$ level, (iii) excitation on the $R_1(0)$ line of the $A^1\Pi, \nu = 0 \leftarrow a^3\Pi_0, \nu = 0$ band, and (iv) spontaneous emission on the $Q(1)$ line of the $A^1\Pi, \nu = 0 \rightarrow X^1\Sigma^+, \nu = 0$ band.

The outcome of the quantum chemistry calculations given in Table V is compared to the experimentally determined values of the hyperfine parameters listed in Table III. The sign and magnitude of the calculated hyperfine parameters are seen to be in good agreement with the experimentally determined ones, with deviations mostly below 5%, although somewhat larger for the c parameters. The relative change of the hyperfine parameters in going from $\nu = 0$ to $\nu = 5$ is also correctly reproduced by the calculations. For the b_F parameters, defined as $b_F = b + c/3$, the latter is less good. This deviation results from the need to keep the c parameter fixed in the fit. The changes of the hyperfine parameters in going from $\nu = 0$ to $\nu = 5$ result predominantly from the concomitant increase of the internuclear distance. The spectroscopic parameters of the $a^3\Pi$ state, in particular the hyperfine structure constants and their variation with the vibrational quantum number, are ideal benchmarks for quantum chemistry calculations.

Although not commonly realized, spectral lines without any broadening due to the finite lifetime of the levels can be obtained in a time-resolved measurement, when the coupled levels have the

TABLE VI. Calculated Franck–Condon factors for the $a^3\Pi$ – $X^1\Sigma^+$ system of AlF.

	$\nu = 0$	$\nu = 1$	$\nu = 2$	$\nu = 3$	$\nu = 4$	$\nu = 5$	$\nu = 6$	$\nu = 7$	$\nu = 8$	$\nu = 9$	$\nu = 10$
$a^3\Pi$											
$\nu = 0$	0.992	$7.5 \cdot 10^{-9}$	$5.8 \cdot 10^{-5}$	$4.6 \cdot 10^{-9}$	$8.8 \cdot 10^{-9}$	$2.3 \cdot 10^{-10}$	$1.2 \cdot 10^{-10}$	$1.0 \cdot 10^{-10}$	$2.1 \cdot 10^{-11}$	$1.9 \cdot 10^{-12}$	$3.4 \cdot 10^{-14}$
$\nu = 1$	0.008	0.976	0.016	$2.0 \cdot 10^{-4}$	$5.8 \cdot 10^{-8}$	$2.3 \cdot 10^{-8}$	$5.4 \cdot 10^{-10}$	$6.0 \cdot 10^{-10}$	$6.2 \cdot 10^{-10}$	$1.4 \cdot 10^{-10}$	$1.4 \cdot 10^{-11}$
$\nu = 2$	$1.2 \cdot 10^{-5}$	0.016	0.958	0.025	$4.0 \cdot 10^{-4}$	$2.8 \cdot 10^{-7}$	$3.4 \cdot 10^{-8}$	$3.7 \cdot 10^{-10}$	$1.7 \cdot 10^{-9}$	$2.0 \cdot 10^{-9}$	$5.3 \cdot 10^{-10}$
$\nu = 3$	$3.0 \cdot 10^{-7}$	$4.7 \cdot 10^{-5}$	0.025	0.938	0.035	$7.4 \cdot 10^{-4}$	$8.8 \cdot 10^{-7}$	$3.9 \cdot 10^{-8}$	$3.9 \cdot 10^{-11}$	$3.5 \cdot 10^{-9}$	$5.2 \cdot 10^{-9}$
$\nu = 4$	$5.9 \cdot 10^{-8}$	$9.6 \cdot 10^{-7}$	$1.2 \cdot 10^{-4}$	0.036	0.916	0.046	0.001	$2.3 \cdot 10^{-6}$	$4.7 \cdot 10^{-8}$	$4.1 \cdot 10^{-9}$	$5.9 \cdot 10^{-9}$
$\nu = 5$	$4.4 \cdot 10^{-9}$	$2.2 \cdot 10^{-7}$	$1.8 \cdot 10^{-6}$	$2.5 \cdot 10^{-4}$	0.047	0.891	0.058	0.002	$5.4 \cdot 10^{-6}$	$7.5 \cdot 10^{-8}$	$2.7 \cdot 10^{-8}$
$\nu = 6$	$1.6 \cdot 10^{-11}$	$1.7 \cdot 10^{-8}$	$5.2 \cdot 10^{-7}$	$2.4 \cdot 10^{-6}$	$4.8 \cdot 10^{-4}$	0.060	0.865	0.072	0.003	$1.2 \cdot 10^{-5}$	$1.8 \cdot 10^{-7}$
$\nu = 7$	$1.3 \cdot 10^{-10}$	$4.7 \cdot 10^{-11}$	$3.7 \cdot 10^{-8}$	$9.9 \cdot 10^{-7}$	$2.3 \cdot 10^{-6}$	$8.4 \cdot 10^{-4}$	0.074	0.835	0.086	0.003	$2.6 \cdot 10^{-5}$
$\nu = 8$	$9.3 \cdot 10^{-11}$	$7.4 \cdot 10^{-10}$	$4.2 \cdot 10^{-11}$	$6.3 \cdot 10^{-8}$	$1.6 \cdot 10^{-6}$	$1.3 \cdot 10^{-6}$	0.001	0.089	0.803	0.101	0.005
$\nu = 9$	$2.4 \cdot 10^{-11}$	$6.0 \cdot 10^{-10}$	$2.3 \cdot 10^{-9}$	$2.8 \cdot 10^{-13}$	$9.2 \cdot 10^{-8}$	$2.5 \cdot 10^{-6}$	$1.5 \cdot 10^{-7}$	0.002	0.105	0.768	0.119
$\nu = 10$	$3.0 \cdot 10^{-12}$	$1.8 \cdot 10^{-10}$	$2.1 \cdot 10^{-9}$	$5.7 \cdot 10^{-9}$	$2.8 \cdot 10^{-10}$	$1.3 \cdot 10^{-7}$	$3.4 \cdot 10^{-6}$	$7.3 \cdot 10^{-7}$	0.003	0.122	0.728
$X^1\Sigma^+$											

same lifetime. By recording an rf transition between Λ -doublet components in the $a^3\Pi_1$ state, we have been able to confirm this. Using an even longer transmission line, thereby increasing the interaction time, this effect can be exploited further.

ACKNOWLEDGMENTS

We thank Marco De Pas, Uwe Hoppe, Sebastian Kray, Christian Schewe, and Klaus-Peter Vogelgesang for excellent technical support and Sid Wright for critical reading of the manuscript. N.W. acknowledges support from the International Max Planck Research School for Elementary Processes in Physical Chemistry. This project received funding from the European Research Council (ERC) under the European Union's Horizon 2020 research and innovation program (CoMoFun, Grant Agreement No. 949119).

AUTHOR DECLARATIONS

Conflict of Interest

The authors declare no conflict of interest.

Author Contributions

N.W. carried out the data acquisition, analyzed and visualized the data, and wrote the manuscript. M.D., S.M., J.S., and S.T. took on parts of the data acquisition. B.G.S. analyzed the data. X.L. and J.P.-R. carried out quantum chemistry calculations. G.M. supervised and conceptualized the project and edited the manuscript.

DATA AVAILABILITY

The data that support the findings of this study are available from the corresponding author upon reasonable request.

APPENDIX A: OBSERVED AND CALCULATED TRANSITION FREQUENCIES

Table VII lists the 30 measured rotational transition frequencies of the $a^3\Pi, \nu \leftarrow X^1\Sigma^+, \nu$ bands. In the first column, the experimentally determined transition frequency $\tilde{\nu}_{\text{exp}}$ is given together with the statistical uncertainty from the Gaussian fit. The systematic experimental uncertainty is estimated to be at maximum 200 MHz, mainly determined by the intrinsic laser profile and the uncertainty of the SBS shift. In the second column, the difference between $\tilde{\nu}_{\text{exp}}$ and the calculated frequency $\tilde{\nu}_{\text{calc}}$ is given. The next columns list the vibrational quantum number ν , the rotational quantum number J , the parity p , and, if applicable, the quantum number Ω of the levels involved in the transition. The indices define whether the quantum numbers belong to the $a^3\Pi$ or to the $X^1\Sigma^+$ state. Only transitions with $\Delta\nu = 0$ are measured. The standard deviation of the fit is 38 MHz.

Table VIII lists the 41 measured rf transition frequencies in the $a^3\Pi_1, \nu = 5$ state. In the first column, the experimentally determined transition frequency f_{exp} is given together with the statistical uncertainty from the Gaussian fit. In the second column, the difference between f_{exp} and the calculated frequency f_{calc} is given. The next columns list the quantum numbers J, F and the parity p of the levels

TABLE VII. Observed and calculated transition frequencies of the $a^3\Pi, \nu \leftarrow X^1\Sigma^+, \nu$ bands. All values are in cm^{-1} .

$\tilde{\nu}_{\text{exp}}$	$\tilde{\nu}_{\text{exp}} - \tilde{\nu}_{\text{calc}}$	ν_a	Ω_a	J_a	p_a	ν_X	J_X	p_X
27 205.553 05(28)	0.0013	0	0	0	+	0	1	-
27 233.829 71(49)	0.0006	1	0	0	+	1	1	-
27 254.149(29)	-0.0020	0	1	4	-	0	4	+
27 254.196(30)	0.0011	0	1	5	+	0	5	-
27 255.172 37(60)	0.0000	0	1	1	-	0	0	+
27 262.453 33(63)	0.0007	2	0	0	+	2	1	-
27 282.544(30)	0.0035	1	1	5	+	1	5	-
27 282.595(30)	-0.0005	1	1	6	-	1	6	+
27 283.502 61(75)	0.0002	1	1	1	-	1	0	+
27 291.376 27(64)	0.0013	3	0	0	+	3	1	-
27 311.182(29)	-0.0023	2	1	4	-	2	4	+
27 311.231(29)	-0.0013	2	1	5	+	2	5	-
27 311.357(30)	-0.0002	2	1	7	+	2	7	-
27 312.177 43(80)	0.0001	2	1	1	-	2	0	+
27 340.130(30)	0.0001	3	1	3	+	3	3	-
27 341.149 59(50)	-0.0003	3	1	1	-	3	0	+
27 349.917 30(53)	0.0001	5	0	0	+	5	1	-
27 369.406(29)	-0.0004	4	1	4	-	4	4	+
27 369.460(29)	0.0007	4	1	5	+	4	5	-
27 369.524(30)	0.0004	4	1	6	-	4	6	+
27 370.371 58(65)	0.0008	4	1	1	-	4	0	+
27 398.842(30)	0.0028	5	1	4	-	5	4	+
27 398.895(30)	-0.0004	5	1	5	+	5	5	-
27 398.964(30)	0.0017	5	1	6	-	5	6	+
27 399.788 38(80)	-0.0005	5	1	1	-	5	0	+
27 428.414(30)	-0.0019	6	1	4	-	6	4	+
27 428.545(30)	-0.0014	6	1	6	-	6	6	+
27 429.351 3(13)	0.0001	6	1	1	-	6	0	+
27 458.035(30)	0.0013	7	1	3	+	7	3	-
27 459.003 3(28)	0.0004	7	1	1	-	7	0	+

involved in the transition. The index n is introduced to distinguish levels with the same values of F and p in order of increasing energy. The lowest energy level for a given combination F, p in the $a^3\Pi$ state gets the index $n = 1$. From the 26 possible transitions in the $J = 1$ level, two overlap within <50 kHz and could not be resolved experimentally and are listed with the same value of f_{exp} . The standard deviation of the fit is 20 kHz.

APPENDIX B: RADIATIVE LIFETIMES IN THE $a^3\Pi, \nu = 0$ STATE

The wavefunctions $|\psi_{\Omega'}(J)\rangle$ for the J levels in the $a^3\Pi_{\Omega'}$ manifolds can be written as

$$|\psi_{\Omega'}(J)\rangle = c_{\Omega',0}(J)|\psi_0(J)\rangle + c_{\Omega',1}(J)|\psi_1(J)\rangle + c_{\Omega',2}(J)|\psi_2(J)\rangle, \quad (\text{B1})$$

with the pure Ω -wavefunctions $|\psi_{\Omega}(J)\rangle$ and the mixing coefficients $c_{\Omega',\Omega}(J)$. The calculated values of $c_{\Omega',\Omega}(J)$ for $J \leq 30$ are listed in Table IX. The squares of the mixing coefficients give the amount of Ω character of a given J level in the $a^3\Pi_{\Omega'}$ manifold, and these are normalized such that

TABLE VIII. Observed and calculated rf transition frequencies in the $a^3\Pi_1, v = 5$ state. All values are in MHz.

f_{exp}	$f_{\text{exp}} - f_{\text{calc}}$	J'	F'	p'	n'	J	F	p	n
1.117(68)	-0.047	1	1	-	1	1	1	+	1
9.960(41)	-0.031	1	2	-	2	1	2	+	2
11.650(18)	0.004	1	3	-	3	1	2	+	2
13.16(63)	-0.015	1	3	+	3	1	3	-	3
20.636(17)	-0.010	1	4	+	4	1	4	-	4
22.533(35)	0.027	1	2	-	2	1	2	+	2
22.876(38)	-0.025	1	3	-	3	1	3	+	3
33.7585(41)	-0.003	1	2	-	2	1	3	+	3
73.163(12)	-0.007	1	4	-	4	1	3	+	3
95.811(13)	0.009	1	1	+	1	1	2	-	2
106.971(52)	0.014	1	1	-	1	1	2	+	2
106.971(52)	-0.023	1	4	+	4	1	3	-	3
126.659(99)	-0.023	1	2	+	2	1	1	-	1
150.411(33)	0.058	1	2	-	2	1	1	+	1
199.588(14)	-0.004	1	3	+	3	1	2	-	2
208.92(13)	-0.005	1	3	-	3	1	2	+	2
210.447(22)	-0.005	1	3	+	3	1	3	-	3
212.42(16)	0.022	1	3	+	3	1	2	-	2
220.19(14)	0.014	1	3	-	3	1	3	+	3
223.638(20)	-0.011	1	2	+	2	1	2	-	2
245.284(14)	-0.001	1	3	-	3	1	2	+	2
256.149(34)	0.004	1	2	-	2	1	2	+	2
304.265(56)	-0.005	1	4	+	4	1	3	-	3
306.520(35)	-0.003	1	4	-	4	1	3	+	3
442.59(30)	0.026	1	3	-	3	1	2	+	2
445.779(56)	0.033	1	3	+	3	1	2	-	2
17.493(26)	0.004	2	3	+	16	2	3	-	16
22.047(35)	0.005	2	2	-	13	2	1	+	8
22.490(25)	-0.027	2	4	-	15	2	4	+	15
36.283(11)	-0.001	2	5	-	13	2	5	+	13
47.681(15)	0.010	2	3	-	15	2	2	+	13
50.892(17)	-0.012	2	3	-	16	2	2	+	14
85.771(13)	0.000	2	4	-	14	2	3	+	15
87.800(19)	0.001	2	0	+	3	2	1	-	8
90.010(11)	0.015	2	5	-	13	2	4	+	15
93.064(58)	-0.032	2	3	+	16	2	2	-	14
94.513(27)	-0.005	2	4	+	15	2	3	-	16
99.515(21)	-0.033	2	4	-	15	2	3	+	16
109.408(16)	0.012	2	3	+	15	2	2	-	13
119.663(26)	0.002	2	5	+	13	2	4	-	14
147.046(28)	-0.002	2	5	-	13	2	4	+	14

$$|c_{\Omega',0}(J)|^2 + |c_{\Omega',1}(J)|^2 + |c_{\Omega',2}(J)|^2 = 1. \quad (\text{B2})$$

The $a^3\Pi$ state interacts with pure singlet states via spin-orbit coupling. For this interaction, the $\Delta\Omega = 0$ selection rule holds. This implies that the strength of the interaction of a given J level with a $^1\Sigma$, a $^1\Pi$ or a $^1\Delta$ state depends on the coefficients $c_{\Omega',0}(J)$, $c_{\Omega',1}(J)$, and $c_{\Omega',2}(J)$, respectively. For the $a^3\Pi$ state of AlF, both mixing with $^1\Sigma^+$ and $^1\Pi$ states is observed. The transition dipole moment $\mu_{a,X}(\Omega', J)$

for transitions from a given $a^3\Pi_{\Omega'}, J$ level to the $X^1\Sigma^+$ electronic ground state can be expressed as

$$\mu_{a,X}(\Omega', J) \propto \kappa c_{\Omega',0}(J) \text{HL}_{\Sigma}(J) + c_{\Omega',1}(J) \text{HL}_{\Pi}(J). \quad (\text{B3})$$

Here, $\text{HL}_{\Sigma}(J)$ and $\text{HL}_{\Pi}(J)$ are the amplitudes of the normalized Hönl-London factors for a $^1\Sigma^+ - ^1\Sigma^+$ and for a $^1\Pi - ^1\Sigma^+$ transition, respectively. The parameter κ is used to quantify the contribution from coupling with a $^1\Sigma^+$ state relative to that with a $^1\Pi$ state; these separate contributions can either interfere constructively

TABLE IX. Calculated mixing coefficients for the wavefunctions of the e and f levels in the Ω manifolds of the $a^3\Pi, v = 0$ state for various values of J .

J	$c_{0,0}$	$c_{0,1}$	$c_{0,2}$	$c_{1,0}$	$c_{1,1}$	$c_{1,2}$	$c_{2,0}$	$c_{2,1}$	$c_{2,2}$
0	1.000 00	0.000 00	0.000 00						
1	0.999 72	-0.023 48	0.000 00	0.023 48	0.999 72	0.000 00			
2	0.999 17	-0.040 63	0.000 69	0.040 63	0.998 59	-0.034 28	0.000 71	0.034 28	0.999 41
3	0.998 35	-0.057 37	0.001 53	0.057 36	0.996 89	-0.054 11	0.001 58	0.054 11	0.998 53
4	0.997 26	-0.073 90	0.002 64	0.073 89	0.994 63	-0.072 43	0.002 73	0.072 42	0.997 37
5	0.995 91	-0.090 26	0.004 02	0.090 26	0.991 84	-0.090 07	0.004 15	0.090 06	0.995 93
6	0.994 30	-0.106 46	0.005 65	0.106 45	0.988 51	-0.107 28	0.005 84	0.107 27	0.994 21
7	0.992 44	-0.122 47	0.007 54	0.122 45	0.984 68	-0.124 15	0.007 78	0.124 14	0.992 23
8	0.990 35	-0.138 28	0.009 67	0.138 26	0.980 35	-0.140 71	0.009 98	0.140 69	0.990 00
9	0.988 02	-0.153 87	0.012 03	0.153 84	0.975 55	-0.156 97	0.012 41	0.156 94	0.987 53
10	0.985 47	-0.169 23	0.014 62	0.169 19	0.970 29	-0.172 93	0.015 08	0.172 89	0.984 83
15	0.969 80	-0.241 97	0.030 52	0.241 86	0.938 10	-0.247 94	0.031 37	0.247 83	0.968 29
20	0.950 39	-0.306 97	0.050 18	0.306 77	0.898 39	-0.314 29	0.051 40	0.314 10	0.948 00
25	0.928 74	-0.363 66	0.072 07	0.363 36	0.854 31	-0.371 64	0.073 58	0.371 35	0.925 57
30	0.906 12	-0.412 23	0.094 90	0.411 84	0.808 50	-0.420 36	0.096 56	0.419 98	0.902 38

TABLE X. Calculated lifetimes for the e and f levels in the Ω manifolds of the $a^3\Pi, v = 0$ state for various values of J , assuming only electric dipole allowed transitions. All values are in ms.

J	$a^3\Pi_0, e$	$a^3\Pi_0, f$	$a^3\Pi_1, e$	$a^3\Pi_1, f$	$a^3\Pi_2, e$	$a^3\Pi_2, f$
0	25.0	∞				
1	24.8	3420	1.89	1.89		
2	24.5	1140	1.89	1.89	1600	1600
3	24.0	573	1.90	1.90	644	644
4	23.4	345	1.91	1.91	359	359
5	22.7	231	1.92	1.92	232	232
6	22.0	166	1.93	1.93	164	164
7	21.1	126	1.94	1.94	122	122
8	20.3	98.6	1.96	1.96	95.2	95.3
9	19.4	79.6	1.98	1.98	76.5	76.6
10	18.5	65.8	2.00	2.00	63.0	63.1
15	14.6	32.2	2.13	2.14	30.7	30.7
20	11.6	20.0	2.32	2.34	19.1	19.1
25	9.56	14.3	2.55	2.58	13.6	13.7
30	8.13	11.1	2.83	2.88	10.6	10.7

($\kappa > 0$) or destructively ($\kappa < 0$). The amplitudes of the normalized Hönl–London factors $HL_{\Pi}(J)$ for $R(J-1)$, $Q(J)$, and $P(J+1)$ transitions are given by

$$\sqrt{\frac{J+1}{2(2J+1)}}, \quad -\frac{1}{\sqrt{2}}, \quad \text{and} \quad \sqrt{\frac{J}{2(2J+1)}}, \quad (\text{B4})$$

respectively. The corresponding normalized amplitudes $HL_{\Sigma}(J)$ are

$$\sqrt{\frac{J}{2J+1}}, \quad 0, \quad \text{and} \quad -\sqrt{\frac{J+1}{2J+1}}. \quad (\text{B5})$$

The ratio of the integrated intensities of the $R_2(0)$ and $R_1(0)$ lines is thus given by

$$\frac{I_{R_2(0)}}{I_{R_1(0)}} = \frac{(\kappa c_{1,0}(1) + c_{1,1}(1))^2}{(\kappa c_{0,0}(1) + c_{0,1}(1))^2}. \quad (\text{B6})$$

The $J = 1, e$ levels in the $a^3\Pi_{\Omega'}$ manifolds can decay via electric dipole transitions to either the $N = 0$ or the $N = 2$ level in the $X^1\Sigma^+$ state thus via the $R_{\Omega'+1}(0)$ or $P_{\Omega'+1}(2)$ line. The total decay rates of these levels for $\Omega' = 0$ and 1 are referred to as γ_0 and γ_1 and their lifetimes as τ_0 and τ_1 , respectively. The ratio of τ_0 and τ_1 is given by

$$\begin{aligned} \frac{\tau_0}{\tau_1} &= \frac{\gamma_1}{\gamma_0} \approx \frac{\tilde{\nu}_{R_2(0)}^3 I_{R_2(0)} + \tilde{\nu}_{P_2(2)}^3 I_{P_2(2)}}{\tilde{\nu}_{R_1(0)}^3 I_{R_1(0)} + \tilde{\nu}_{P_1(2)}^3 I_{P_1(2)}} \\ &\approx \frac{(\kappa c_{1,0}(1) + c_{1,1}(1))^2 + 2(-\kappa c_{1,0}(1) + 0.5 c_{1,1}(1))^2}{(\kappa c_{0,0}(1) + c_{0,1}(1))^2 + 2(-\kappa c_{0,0}(1) + 0.5 c_{0,1}(1))^2}, \quad (\text{B7}) \end{aligned}$$

where $\tilde{\nu}$ is the transition frequency and I is the transition intensity of the line given by the respective index. In the first approximation of Eq. (B7), it is assumed that the Franck–Condon factor for the $a^3\Pi, v = 0 \rightarrow X^1\Sigma^+, v = 0$ transition is exactly 1.0, and in the second approximation, the frequencies of the various transitions are taken to be equal.

The observed intensity ratio $I_{R_2(0)}/I_{R_1(0)} = 20.9 \pm 1.0$ is consistent with both $\kappa_+ = 0.243 \pm 0.013$ and $\kappa_- = -0.194 \pm 0.011$, resulting in ratios of $\tau_0/\tau_1 = 8.4 \pm 0.7$ and $\tau_0/\tau_1 = 13.2 \pm 1.1$, respectively. The observation that the P_1 lines are considerably weaker than the R_1 lines¹³ is only consistent with the case of destructive interference, i.e., $\kappa = \kappa_-$.

REFERENCES

- J. L. Bohn, A. M. Rey, and J. Ye, “Cold molecules: Progress in quantum engineering of chemistry and quantum matter,” *Science* **357**, 1002–1010 (2017).
- B. R. Heazlewood and T. P. Soffley, “Towards chemistry at absolute zero,” *Nat. Rev. Chem.* **5**, 125–140 (2021).

- ³S. Y. T. van de Meerakker, H. L. Bethlem, N. Vanhaecke, and G. Meijer, "Manipulation and control of molecular beams," *Chem. Rev.* **112**, 4828–4878 (2012).
- ⁴C. Chin, V. V. Flambaum, and M. G. Kozlov, "Ultracold molecules: New probes on the variation of fundamental constants," *New J. Phys.* **11**, 055048 (2009).
- ⁵J. J. Hudson, D. M. Kara, I. J. Smallman, B. E. Sauer, M. R. Tarbutt, and E. A. Hinds, "Improved measurement of the shape of the electron," *Nature* **473**, 493–496 (2011).
- ⁶J. Baron, W. C. Campbell, D. DeMille, J. M. Doyle, G. Gabrielse, Y. V. Gurevich, P. W. Hess, N. R. Hutzler, E. Kirilov, I. Kozyryev, B. R. O'Leary, C. D. Panda, M. F. Parsons, E. S. Petrik, B. Spaun, A. C. Vutha, and A. D. West, "Order of magnitude smaller limit on the electric dipole moment of the electron," *Science* **343**, 269–272 (2014).
- ⁷W. B. Cairncross, D. N. Gresh, M. Grau, K. C. Cossel, T. S. Roussy, Y. Ni, Y. Zhou, J. Ye, and E. A. Cornell, "Precision measurement of the electron's electric dipole moment using trapped molecular ions," *Phys. Rev. Lett.* **119**, 153001 (2017).
- ⁸V. Andreev, D. G. Ang, D. DeMille, J. M. Doyle, G. Gabrielse, J. Haefner, N. R. Hutzler, Z. Lasner, C. Meisenhelder, B. R. O'Leary, C. D. Panda, A. D. West, E. P. West, and X. Wu, "Improved limit on the electric dipole moment of the electron," *Nature* **562**, 355–360 (2018).
- ⁹D. DeMille, "Quantum computation with trapped polar molecules," *Phys. Rev. Lett.* **88**, 067901 (2002).
- ¹⁰A. Micheli, G. K. Brennen, and P. Zoller, "A toolbox for lattice-spin models with polar molecules," *Nat. Phys.* **2**, 341–347 (2006).
- ¹¹R. Sawant, J. A. Blackmore, P. D. Gregory, J. Mur-Petit, D. Jaksch, J. Aldegunde, J. M. Hutson, M. R. Tarbutt, and S. L. Cornish, "Ultracold polar molecules as qubits," *New J. Phys.* **22**, 013027 (2020).
- ¹²M. D. Di Rosa, "Laser-cooling molecules—Concept, candidates, and supporting hyperfine-resolved measurements of rotational lines in the A–X(0,0) band of CaH," *Eur. Phys. J. D* **31**, 395–402 (2004).
- ¹³S. Truppe, S. Marx, S. Kray, M. Doppelbauer, S. Hofsäss, H. C. Schewe, N. Walter, J. Pérez-Ríos, B. G. Sartakov, and G. Meijer, "Spectroscopic characterization of aluminum monofluoride with relevance to laser cooling and trapping," *Phys. Rev. A* **100**, 052513 (2019).
- ¹⁴S. Hofsäss, M. Doppelbauer, S. C. Wright, S. Kray, B. G. Sartakov, J. Pérez-Ríos, G. Meijer, and S. Truppe, "Optical cycling of AlF molecules," *New J. Phys.* **23**, 075001 (2021).
- ¹⁵N. Wells and I. C. Lane, "Electronic states and spin-forbidden cooling transitions of AlH and AlF," *Phys. Chem. Chem. Phys.* **13**, 19018–19025 (2011).
- ¹⁶M. Yousefi and P. F. Bernath, "Line lists for AlF and AlCl in the $X^1\Sigma^+$ ground state," *Astrophys. J., Suppl. Ser.* **237**, 8 (2018).
- ¹⁷R. F. Barrow, I. Kopp, and C. Malmberg, "The electronic spectrum of gaseous AlF," *Phys. Scr.* **10**, 86–102 (1974).
- ¹⁸J. M. Brown, I. Kopp, C. Malmberg, and B. Rydh, "An analysis of hyperfine interactions in the electronic spectrum of AlF," *Phys. Scr.* **17**, 55–67 (1978).
- ¹⁹S. Rosenwaks, R. E. Steele, and H. P. Broida, "Observation of $a^3\Pi-X^1\Sigma^+$ intercombination emission in AlF," *Chem. Phys. Lett.* **38**, 121–124 (1976).
- ²⁰T. C. James, "Transition moments, Franck—Condon factors, and lifetimes of forbidden transitions. Calculation of the intensity of the Cameron system of CO," *J. Chem. Phys.* **55**, 4118–4124 (1971).
- ²¹N. Walter, J. Seifert, S. Truppe, H. C. Schewe, B. G. Sartakov, and G. Meijer, "Spectroscopic characterization of singlet triplet doorway states of aluminum monofluoride," *arXiv:2202.07920* (2022).
- ²²M. Doppelbauer, N. Walter, S. Hofsäss, S. Marx, H. C. Schewe, S. Kray, J. Pérez-Ríos, B. G. Sartakov, S. Truppe, and G. Meijer, "Characterisation of the $b^3\Sigma^+$, $v = 0$ state and its interaction with the $A^1\Pi$ state in aluminium monofluoride," *Mol. Phys.* **119**, e1810351 (2021).
- ²³K. Huber and G. Herzberg, *Molecular Spectra and Molecular Structure. IV. Constants of Diatomic Molecules* (Springer, Van Nostrand Reinhold, New York, 1979).
- ²⁴K. Q. Zhang, B. Guo, V. Braun, M. Dulick, and P. F. Bernath, "Infrared emission spectroscopy of BF and AlF," *J. Mol. Spectrosc.* **170**, 82–93 (1995).
- ²⁵J. M. Brown and A. J. Merer, "Lambda-type doubling parameters for molecules in Π electronic states of triplet and higher multiplicity," *J. Mol. Spectrosc.* **74**, 488–494 (1979).
- ²⁶R. W. Field, S. G. Tilford, R. A. Howard, and J. D. Simmons, "Fine structure and perturbation analysis of the $a^3\Pi$ state of CO," *J. Mol. Spectrosc.* **44**, 347–382 (1972).
- ²⁷I. Kopp, B. Lindgren, and C. Malmberg, "Rotational analysis of the $a^3\Pi-X^1\Sigma^+$ transition of AlF," *Phys. Scr.* **14**, 170–174 (1976).
- ²⁸R. J. Le Roy, "dPotFit: A computer program to fit diatomic molecule spectral data to potential energy functions," *J. Quant. Spectrosc. Radiat. Transfer* **186**, 179–196 (2017).
- ²⁹R. J. Le Roy and A. Pashov, "betaFIT: A computer program to fit pointwise potentials to selected analytic functions," *J. Quant. Spectrosc. Radiat. Transfer* **186**, 210–220 (2017).
- ³⁰R. J. Le Roy, "RKR1: A computer program implementing the first-order RKR method for determining diatomic molecule potential energy functions," *J. Quant. Spectrosc. Radiat. Transfer* **186**, 158–166 (2017).
- ³¹B. Girard, G. O. Sitz, R. N. Zare, N. Billy, and J. Vigué, "Polarization dependence of the AC Stark effect in multiphoton transitions of diatomic molecules," *J. Chem. Phys.* **97**, 26–41 (1992).
- ³²J. J. Gilijamse, S. Hoekstra, S. A. Meek, M. Metsälä, S. Y. T. van de Meerakker, G. Meijer, and G. C. Groenenboom, "The radiative lifetime of metastable CO ($a^3\Pi$, $v = 0$)," *J. Chem. Phys.* **127**, 221102 (2007).
- ³³N. S. Mosyagin, A. V. Oleynichenko, A. Zaitsevskii, A. V. Kudrin, E. A. Pazyuk, and A. V. Stolyarov, "Ab initio relativistic treatment of the $a^3\Pi-X^1\Sigma^+$, $a^3\Sigma^+-X^1\Sigma^+$ and $A^1\Pi-X^1\Sigma^+$ systems of the CO molecule," *J. Quant. Spectrosc. Radiat. Transfer* **263**, 107532 (2021).
- ³⁴R. T. Jongma, G. Berden, and G. Meijer, "State-specific lifetime determination of the $a^3\Pi$ state in CO," *J. Chem. Phys.* **107**, 7034–7040 (1997).
- ³⁵M. J. Frisch, G. W. Trucks, H. B. Schlegel, G. E. Scuseria, M. A. Robb, J. R. Cheeseman, G. Scalmani, V. Barone, G. A. Petersson, H. Nakatsuji, X. Li, M. Caricato, A. V. Marenich, J. Bloino, B. G. Janesko, R. Gomperts, B. Mennucci, H. P. Hratchian, J. V. Ortiz, A. F. Izmaylov, J. L. Sonnenberg, D. Williams-Young, F. Ding, F. Lipparini, F. Egidi, J. Goings, B. Peng, A. Petrone, T. Henderson, D. Ranasinghe, V. G. Zakrzewski, J. Gao, N. Rega, G. Zheng, W. Liang, M. Hada, M. Ehara, K. Toyota, R. Fukuda, J. Hasegawa, M. Ishida, T. Nakajima, Y. Honda, O. Kitao, H. Nakai, T. Vreven, K. Throssell, J. A. Montgomery, Jr., J. E. Peralta, F. Ogliaro, M. J. Bearpark, J. J. Heyd, E. N. Brothers, K. N. Kudin, V. N. Staroverov, T. A. Keith, R. Kobayashi, J. Normand, K. Raghavachari, A. P. Rendell, J. C. Burant, S. S. Iyengar, J. Tomasi, M. Cossi, J. M. Millam, M. Klene, C. Adamo, R. Cammi, J. W. Ochterski, R. L. Martin, K. Morokuma, O. Farkas, J. B. Foresman, and D. J. Fox, GAUSSIAN 16, Revision C.01, 2016.
- ³⁶T. Yanai, D. P. Tew, and N. C. Handy, "A new hybrid exchange–correlation functional using the Coulomb-attenuating method (CAM-B3LYP)," *Chem. Phys. Lett.* **393**, 51–57 (2004).
- ³⁷T. H. Dunning, "Gaussian basis sets for use in correlated molecular calculations. I. The atoms boron through neon and hydrogen," *J. Chem. Phys.* **90**, 1007–1023 (1989).
- ³⁸R. A. Kendall, T. H. Dunning, and R. J. Harrison, "Electron affinities of the first-row atoms revisited. Systematic basis sets and wave functions," *J. Chem. Phys.* **96**, 6796–6806 (1992).
- ³⁹D. E. Woon and T. H. Dunning, "Gaussian basis sets for use in correlated molecular calculations. III. The atoms aluminum through argon," *J. Chem. Phys.* **98**, 1358–1371 (1993).
- ⁴⁰J. Bieroń, P. Pyykkö, D. Sundholm, V. Kellö, and A. J. Sadlej, "Nuclear quadrupole moments of bromine and iodine from combined atomic and molecular data," *Phys. Rev. A* **64**, 052507 (2001).
- ⁴¹A. Aerts and A. Brown, "A revised nuclear quadrupole moment for aluminum: Theoretical nuclear quadrupole coupling constants of aluminum compounds," *J. Chem. Phys.* **150**, 224302 (2019).

⁴²P. Pyykkö, “Year-2017 nuclear quadrupole moments,” *Mol. Phys.* **116**, 1328–1338 (2018).

⁴³J. C. Light, I. P. Hamilton, and J. V. Lill, “Generalized discrete variable approximation in quantum mechanics,” *J. Chem. Phys.* **82**, 1400–1409 (1985).

⁴⁴J. V. Lill, G. A. Parker, and J. C. Light, “Discrete variable representations and sudden models in quantum scattering theory,” *Chem. Phys. Lett.* **89**, 483–489 (1982).

⁴⁵G. C. Dousmanis, T. M. Sanders, and C. H. Townes, “Microwave spectra of the free radicals OH and OD,” *Phys. Rev.* **100**, 1735–1754 (1955).

⁴⁶H. Figger and H. Walther, “Optical resolution beyond the natural linewidth: A level-crossing experiment on the $3^2P_{3/2}$ level of sodium using a tunable dye laser,” *Z. Phys.* **267**, 1–8 (1974).

⁴⁷A. I. Burshtein and A. V. Storozhev, “Transition width between two metastable states,” *Chem. Phys.* **119**, 1–13 (1988).